Simulation of O^+ upflows created by electron precipitation and Alfvén waves in the ionosphere

D. Sydorenko[1] and R. Rankin[1]

Received 19 March 2013; revised 21 August 2013; accepted 22 August 2013; published 10 September 2013.

[1] A two-dimensional model of magnetosphere-ionosphere coupling is presented. It includes Alfvén wave dynamics, ion motion along the geomagnetic field, chemical reactions between ions and neutrals, collisions between different species, and a parametric model of electron precipitation. Representative simulations are presented, along with a discussion of the physical mechanisms that are important in forming oxygen ion field-aligned plasma flows. In particular, it is demonstrated that ion upwelling is strongly affected by the ponderomotive force of standing Alfvén waves in the ionospheric Alfvén resonator, and by enhanced electric fields that are produced when electrons are heated by soft electron precipitation. It is verified that the simulations are in qualitative agreement with available theoretical predictions. In the resonator, in addition to the ponderomotive force, a contribution to the upflow comes from centrifugal acceleration. Heating by the current of standing waves increases parallel electric fields and ion pressure gradients only at low altitudes where they are easily balanced by friction with neutrals. This prevents development of fast field-aligned ion flows in the *E*-layer and lower *F*-layer.

Citation: Sydorenko, D., and R. Rankin (2013), Simulation of O^+ upflows created by electron precipitation and Alfvén waves in the ionosphere, *J. Geophys. Res. Space Physics*, *118*, 5562–5578, doi:10.1002/jgra.50531.

1. Introduction

[2] Ionospheric ion upwelling and outflow is important in the context of its influence on the global dynamics of magnetospheric plasma. The processes controlling ion outflow are numerous and include precipitation of energetic particles from the magnetosphere to the ionosphere, transverse ion energization by electromagnetic waves, field-aligned currents and ionospheric Joule heating, chemical reactions, solar radiation, and Alfvén wave dissipation [*Yau et al.*, 2007]. This paper presents a numerical model of the coupled magnetosphere and ionosphere that accounts for many of these processes through further development of the model of *Sydorenko and Rankin* [2012], which did not consider ion dynamics along geomagnetic field lines. The additional physical processes and representative results from the model are described below.

[3] In the model of *Sydorenko and Rankin* [2012], field-aligned ion motion in the ionosphere is omitted. This simplification is made because a stationary initial state of the ionosphere is then relatively easy to achieve. A second reason is that in describing reflection of waves from the ionosphere, it is not necessary to account for slow density changes caused by large-scale field-aligned plasma motion. The drawback is that the model is limited to low-current regimes when vertical ionospheric ion flows are not important. This, in particular, makes it impractical to include chemical reactions and electron precipitation.

[4] Unlike the model of [*Sydorenko and Rankin*, 2012], which solved different sets of equations in the ionosphere and magnetosphere for numerical efficiency, the extension of the model presented here uses the same set of plasma dynamics equations at all altitudes in the main simulation area. The importance of this is that the transition over altitude from collisional to collisionless plasma dynamics is ensured by a gradual (physical) decrease of collision frequencies with altitude rather than a discontinuous change. It also means that chemical reactions and a parametric model of electron precipitation originally developed for the model of *Sydorenko and Rankin* [2012] can be enabled without unphysical behavior arising.

[5] In the results presented below, capabilities of the new model are tested through simulations in which O^+ ion upflows are created by electron precipitation or by Alfvén waves. In the case of electron precipitation, ion upflows are usually attributed to electron heating and the related enhancement of field-aligned ambipolar electric fields [*Strangeway et al.*, 2005]. There is also observational [*Seo et al.*, 1997] and numerical [e.g., *Su et al.*, 1999; *Vontrat-Reberac et al.*, 2001] evidence that ion upflows are created more effectively by electron precipitation with relatively low energy. The present model agrees with these results and shows quantitatively that high-energy precipitation deposits its energy at lower altitudes where intense

[1]Department of Physics, University of Alberta, Edmonton, Alberta, Canada.

Corresponding author: D. Sydorenko, Department of Physics, University of Alberta, 4-181 CCIS, Edmonton, Alberta, T6G 2E1, Canada. (sydorenk@ualberta.ca)

2169-9380/13/10.1002/jgra.50531

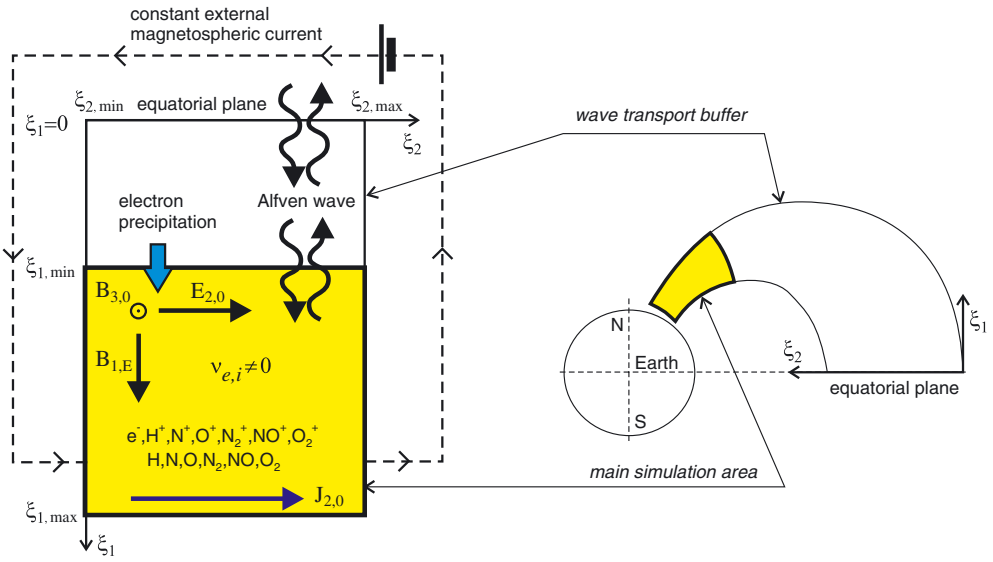

Figure 1. Schematic of the simulated ionosphere-magnetosphere system in (left) dipole coordinates and (right) real space.

cooling prevents a long-lasting increase of the electron temperature.

[6] Ion upflows can be driven effectively by the ponderomotive force of standing Alfvén waves. Of interest here is relatively high frequency (1–10 Hz) standing waves in the ionospheric Alfvén resonator, which have previously been shown to create field-aligned ion flows [*Streltsov and Lotko*, 2008]. The present model shows formation of ion upflows above 500 km due to this effect. Upflowing ions also appear when there is intense frictional ion heating due to plasma convection [*Wahlund et al.*, 1992] or large-scale magnetospheric currents [*Strangeway et al.*, 2005]. Such currents may also be associated with low-frequency (0.1 Hz and less) Alfvén waves, but a discussion of low-frequency waves is deferred for future study.

[7] The model of *Sydorenko and Rankin* [2012] describes the ionosphere following [*Schunk*, 1988]. Below, these papers are mentioned frequently; so for brevity, the paper of *Sydorenko and Rankin* [2012] is referred to as SR12 and the paper of *Schunk* [1988] is referred to as S88 henceforth.

[8] The paper is organized as follows. In section 2, a brief description of the model is given and the main equations are listed. In section 3, excitation of ion upflows by low-energy and high-energy electron precipitation is discussed. Section 4 considers ion upflows created by a standing Alfvén wave in the ionospheric Alfvén resonator. Concluding remarks are given in section 5. Appendix A describes the parametric model of electron precipitation. Appendix B clarifies changes to the boundary conditions compared to SR12. Appendix C contains parameters of the numerical grid. The procedure of calculation of the initial state is given in Appendix D.

2. Numerical Model of the Ionosphere

[9] The model presented considers a relatively narrow two-dimensional (2-D) region in near-Earth space enclosed between two geomagnetic field lines (see Figure 1). The geomagnetic field is dipole; the dipole coordinates are $\xi_1 = \cos\vartheta/r^2$, $\xi_2 = \sin^2\vartheta/r$, and $\xi_3 = -\varphi$, where $\{r, \vartheta, \varphi\}$ are the usual spherical coordinates. Azimuthal symmetry is assumed. The top and the bottom boundaries of the simulation domain are surfaces of constant dipole coordinate ξ_1. In order to avoid large deviation of the bottom boundary from spherical shape, the width of the simulated area at the bottom end is limited to a few hundred kilometers. For the same reason, the bottom boundary should be at high latitudes.

[10] The main simulation area includes the ionosphere and the lower magnetosphere. The plasma inside the main simulation area consists of electrons and H^+, N^+, O^+, N_2^+, NO^+, and O_2^+ ions. The electrons and the ions collide with each other and with H, N, O, N_2, NO, and O_2 neutrals. The bottom boundary of the main simulation area is typically at an altitude of about 100 km, whereas the top boundary is at an altitude of a few thousand kilometers. Chemical reactions between ions and neutrals are accounted for. The plasma in the main simulation area can be perturbed by electron precipitation or an Alfvén wave injected through the top boundary. A meridional wind with nonuniform altitude profile of velocity can also be introduced. For simplicity, it is assumed that the wind blows exactly along the ξ_2-direction. In simulations described below, the wind velocity is zero.

[11] A second component of the simulation domain, the wave transport buffer, stretches from the top of the main simulation area to the equatorial plane. This buffer provides nonreflecting boundary conditions for Alfvén waves and allows slow variation of the background electric and magnetic fields.

[12] The numerical scheme of the present model is the same as in SR12. It includes (i) an implicit quasi-neutral 2-D electromagnetic solver optimized for shear Alfvén waves, (ii) a semi-Lagrangian method of solving the continuity and pressure equations, (iii) a nonuniform grid, (iv) boundary conditions at the top and bottom boundaries of the main simulation area, and (v) the wave transport buffer. Many equations listed in SR12 have been modified to include additional terms due to collisional field-aligned ion motion. The boundary conditions at the southern and northern boundaries

(geomagnetic field lines) have been changed as well. For convenience, the full set of equations for the main simulation area is given below.

[13] Note that in the present paper, subscript e denotes electrons, subscript α denotes ion species (α can be H^+, N^+, O^+, N_2^+, NO^+, and O_2^+), subscript α' denotes ion species different from ion species α, subscript γ denotes both electrons and ions (γ can be e or any of α), and subscript β denotes neutrals (β can be H, N, O, N_2, NO, and O_2). Vector values directed along geomagnetic field lines are referred to as the parallel ones. Vectors directed in the ξ_2-direction (meridional) are referred to as the transverse ones.

2.1. Electromagnetic Field

[14] The electromagnetic field components E_1, E_2, and B_3 are calculated from the following equations:

$$\frac{1}{c^2}\frac{\partial E_2}{\partial t} = -\frac{1}{h_1 h_3}\frac{\partial h_3 B_3}{\partial \xi_1} - \mu_0 J_2 \,, \tag{1}$$

$$\frac{\partial B_3}{\partial t} = \frac{1}{h_1 h_2}\left(\frac{\partial h_1 E_1}{\partial \xi_2} - \frac{\partial h_2 E_2}{\partial \xi_1}\right) \tag{2}$$

$$\begin{aligned} E_1 \sum_{\gamma=e,\alpha}\frac{n_\gamma e^2}{m_\gamma} = {} & \sum_{\gamma=e,\alpha} q_\gamma \left\{\frac{1}{h_1}\frac{\partial}{\partial \xi_1}\left(\frac{p_\gamma}{m_\gamma}\right) + n_\gamma\left[(\mathbf{u}_\gamma\cdot\nabla)\mathbf{u}_\gamma\right]_1 \right. \\ & \left. - u_{\gamma,1}\frac{\partial n_\gamma}{\partial t}\right\} - \sum_\alpha \frac{n_\alpha e^2}{m_\alpha} u_{\alpha,2} B_3 + \frac{\partial J_1}{\partial t} \\ & - e n_e\left[\sum_\beta \nu_{e,\beta} u_{e,1} + \sum_\alpha \nu_{e,\alpha}\left(1+\frac{m_e}{m_\alpha}\right)(u_{e,1}-u_{\alpha,1})\right] \\ & + e\sum_\alpha n_\alpha\left[\sum_\beta \nu_{\alpha,\beta}u_{\alpha,1} + \sum_{\alpha'}^{\alpha'\neq\alpha}\nu_{\alpha,\alpha'}(u_{\alpha,1}-u_{\alpha',1})\right], \end{aligned} \tag{3}$$

$$\frac{\partial}{\partial \xi_1}(J_1 h_2 h_3) + \frac{\partial}{\partial \xi_2}(J_2 h_1 h_3) = 0 \,, \tag{4}$$

where c is the light speed, e is the elementary charge (positive), q_γ, m_γ, n_γ, p_γ, and $\mathbf{u}_\gamma$ are the charge, mass, number density, pressure, and vector velocity of charged species, $q_e = -e$, $q_\alpha = e$, $J_{1,2}$ are the electric current components, $J_1 = J_1^{pr} + \sum_{\gamma=e,\alpha} q_\gamma n_\gamma u_{\gamma,1}$, J_1^{pr} is the electric current due to precipitating electrons, which is an externally defined function of time and space (see Appendix A). The second term in the right-hand side (RHS) of the definition of J_1 is due to the parallel motion of ionospheric electrons and ions and is self-consistent, $J_2 = \sum_\alpha q_\alpha n_\alpha u_{\alpha,2}$. Note that although equation (1) is written in a traditional form with the displacement current in the left-hand side, it is the polarization part of the transverse current J_2 which contains the largest term proportional to $\partial E_2/\partial t$ (see equation (6)). The convective velocity derivative terms $[(\mathbf{u}_\gamma\cdot\nabla)\mathbf{u}_\gamma]_1$ are defined below. The dipole metric factors $h_{1,2,3}$ are $h_2 = r^2/(\sin\vartheta\sqrt{1+3\cos^2\vartheta})$, $h_3 = r\sin\vartheta$, and $h_1 = h_2 h_3$. In (3), the following momentum transfer collision frequencies are used: $\nu_{e,\beta}$ for collisions between electrons and neutrals β (defined in Table 1 of S88), $\nu_{e,\alpha}$ for Coulomb collisions between electrons and ions α (defined in equation (7) of S88), $\nu_{\alpha,\beta}$ for collisions between ions α and neutrals β (defined in Tables 3, 4, and equation (9) of S88), and $\nu_{\alpha,\alpha'}$ for Coulomb collisions between ions α and ions α' (defined in Table 2 and equation (8) of S88).

2.2. Ion Dynamics

[15] The dynamics of ions α is described by the following equations:

$$\begin{aligned} \frac{\partial u_{\alpha,1}}{\partial t} = {} & -\left[(\mathbf{u}_\alpha\cdot\nabla)\mathbf{u}_\alpha\right]_1 + \frac{e}{m_\alpha}(E_1 + u_{\alpha,2}B_3) \\ & - \frac{1}{m_\alpha n_\alpha h_1}\frac{\partial}{\partial \xi_1}p_\alpha + g_1 \\ & - \sum_\beta \nu_{\alpha,\beta}u_{\alpha,1} - \sum_{\alpha'\neq\alpha}\nu_{\alpha,\alpha}(u_{\alpha,1}-u_{\alpha',1}) \\ & - \nu_{\alpha,e}(u_{\alpha,1}-u_{e,1}) \,, \end{aligned} \tag{5}$$

$$u_{\alpha,2} = \frac{1}{1+\nu_\alpha^2/\Omega_\alpha^2}\frac{m_\alpha}{eB_E^2}\left(\frac{\partial E_2}{\partial t} + \nu_\alpha E_2\right) + \frac{\nu_\alpha^2/\Omega_\alpha^2}{1+\nu_\alpha^2/\Omega_\alpha^2}w_2 \,, \tag{6}$$

$$u_{\alpha,3} = -\frac{1}{1+\nu_\alpha^2/\Omega_\alpha^2}\frac{E_2}{B_E} - \frac{\nu_\alpha/\Omega_\alpha}{1+\nu_\alpha^2/\Omega_\alpha^2}w_2 \,, \tag{7}$$

$$\begin{aligned} \left(\frac{\partial}{\partial t} + \frac{u_{\alpha,1}}{h_1}\frac{\partial}{\partial \xi_1} + \frac{u_{\alpha,2}}{h_2}\frac{\partial}{\partial \xi_2}\right)n_\alpha = {} & -\frac{n_\alpha}{h_1 h_2 h_3}\left(\frac{\partial}{\partial \xi_1}u_{\alpha,1}h_2 h_3 \right. \\ & \left. + \frac{\partial}{\partial \xi_2}u_{\alpha,2}h_1 h_3\right) + \sum_\beta r_{\beta,\alpha} + \sum_{\beta,\alpha'}P^\alpha_{\beta,\alpha'} - \sum_{\beta,\alpha'}P^{\alpha'}_{\beta,\alpha} \,, \end{aligned} \tag{8}$$

$$\begin{aligned} \left(\frac{\partial}{\partial t} + \frac{u_{\alpha,1}}{h_1}\frac{\partial}{\partial \xi_1} + \frac{u_{\alpha,2}}{h_2}\frac{\partial}{\partial \xi_2}\right)p_\alpha = {} & -\frac{5}{3}\frac{p_\alpha}{h_1 h_2 h_3}\left(\frac{\partial}{\partial \xi_1}u_{\alpha,1}h_2 h_3 \right. \\ & \left. + \frac{\partial}{\partial \xi_2}u_{\alpha,2}h_1 h_3\right) - \frac{2}{3h_1 h_2 h_3}\frac{\partial}{\partial \xi_1}q_{\alpha,1}h_2 h_3 \\ & + 2n_\alpha\sum_\beta \frac{m_\alpha \nu_{\alpha,\beta}}{m_\alpha+m_\beta}(T_n - T_i) + 2n_e\frac{m_e\nu_{e,\alpha}}{m_\alpha+m_e}(T_e - T_i) \\ & + \frac{2}{3}n_\alpha\sum_\beta \frac{m_\alpha m_\beta \nu_{\alpha,\beta}}{m_\alpha+m_\beta}[u_{\alpha,1}^2 + (u_{\alpha,2}-w_2)^2 + u_{\alpha,3}^2] \\ & + \frac{2}{3}n_\alpha\sum_{\alpha'\neq\alpha}\frac{m_\alpha m'_\alpha \nu_{\alpha,\alpha'}}{m_\alpha+m'_\alpha}(u_{\alpha,1}-u_{\alpha',1})^2 \\ & + \sum_\beta r_{\beta,\alpha}T_n + \sum_{\beta,\alpha'}P^\alpha_{\beta,\alpha'}Q^\alpha_{\beta,\alpha'} - \sum_{\beta,\alpha'}P^{\alpha'}_{\beta,\alpha}T_i \,. \end{aligned} \tag{9}$$

where

$$\begin{aligned} \left[(\mathbf{u}_\alpha\cdot\nabla)\mathbf{u}_\alpha\right]_1 = {} & \frac{u_{\alpha,1}}{h_1}\frac{\partial u_{\alpha,1}}{\partial \xi_1} + \frac{u_{\alpha,2}}{h_2}\frac{\partial u_{\alpha,1}}{\partial \xi_2} + \frac{u_{\alpha,1}u_{\alpha,2}}{2h_1^2 h_2}\frac{\partial h_1^2}{\partial \xi_2} \\ & - \frac{u_{\alpha,2}^2}{2h_1 h_2^2}\frac{\partial h_2^2}{\partial \xi_1} - \frac{u_{\alpha,3}^2}{2h_1 h_3^2}\frac{\partial h_3^2}{\partial \xi_1} \,, \end{aligned} \tag{10}$$

g_1 is the acceleration due to the gravity force along the geomagnetic field, $\nu_\alpha = \sum_\beta \nu_{\alpha,\beta}$, $\Omega_\alpha = q_\alpha B_E/m_\alpha$, B_E is the geomagnetic field, w_2 is the meridional neutral wind velocity, $r_{\beta,\alpha}$ is the rate of production of ions α from neutrals β by electron precipitation (see equation (A3)), $P^\alpha_{\beta,\alpha'}$ is the rate of production of ions α due to chemical reactions between neutrals β and ions α' (the chemical reactions are described in Table 1 in *Blelly et al.* [1996]), $q_{\alpha,1}$ is the ion heat flow, and T_e, T_i, and T_n are the electron, ion, and neutral gas temperatures. The neutral temperature is constant in time. The electron temperature is calculated as $T_e = p_e/n_e$. At each time step, the updated ion temperature is calculated from updated ion pressures p_α and densities n_α as $T_i = \sum_\alpha p_\alpha / \sum_\alpha n_\alpha$; then the ion pressures are reset to $p_\alpha = n_\alpha T_i$ (see more details in SR12).

[16] Note that calculation of the ion heat flow in a plasma with multiple ion species is a cumbersome task [*Zhdanov*, 2002]. It simplifies greatly if one assumes that the ion heat

flow is significant only at higher altitudes (above few hundred kilometers), where collisions are infrequent. At these altitudes, the major ion species is O^+. Then, it is sufficient to find only the heat flow of O^+ ions, which can be done using expressions for a single ion species plasma given in S88.

[17] The last three terms in (9) describe ion pressure modification due to ion production by ionization, ion heating in chemical reactions, and loss of ions in chemical reactions, respectively. In the chemical reaction heating term, $Q^{\alpha}_{\beta,\alpha'}$ is the energy acquired by ion α when it is produced in a chemical reaction between neutral β and ion α'. The latter is calculated as $Q^{\alpha}_{\beta,\alpha'} = \delta^{\alpha}_{\beta,\alpha'}[1 - m_\alpha/(m_\beta + m'_\alpha)]$, where $\delta^{\alpha}_{\beta,\alpha'}$ is the energy output of a reaction between neutral β and ion α' producing ion α. The values of $\delta^{\alpha}_{\beta,\alpha'}$ for the reactions described in Table 1 of *Blelly et al.* [1996] can be found in Table 2 of *Tian et al.* [2008].

[18] For completeness, it is necessary to mention that chemical reactions change the densities of neutrals as well. For the parameters of simulations selected in the present paper, the related modification of the neutral densities is a minor effect. Below 800 km altitude, the densities remain very close to their initial values. At higher altitudes, there is a noticeable growth of the density of O due to the charge-exchange reaction between O^+ and H. The frequency of ion collisions here, however, remains very low and does not affect the ion dynamics (see the solid red curve above 800 km in Figure 13d).

2.3. Electron Dynamics

[19] The electron dynamics is described by the following equations:

$$\frac{\partial u_{e,1}}{\partial t} = -[(\mathbf{u}_e\cdot\nabla)\mathbf{u}_e]_1 - \frac{e}{m_e}E_1 - \frac{1}{m_e n_e h_1}\frac{\partial}{\partial \xi_1}p_e + g_1 - \sum_\beta \nu_{e,\beta}u_{e,1} - \sum_\alpha \nu_{e,\alpha}(u_{e,1}-u_{\alpha,1})\,, \tag{11}$$

$$u_{e,2} = 0\,, \tag{12}$$

$$u_{e,3} = -\frac{E_2}{B_E}\,, \tag{13}$$

$$n_e = \sum_\alpha n_\alpha\,, \tag{14}$$

$$\left(\frac{\partial}{\partial t} + \frac{u_{e,1}}{h_1}\frac{\partial}{\partial \xi_1}\right)p_e = -\frac{5}{3}\frac{p_e}{h_1h_2h_3}\frac{\partial}{\partial\xi_1}u_{e,1}h_2h_3 - \frac{2}{3h_1h_2h_3}\frac{\partial}{\partial\xi_1}q_{e,1}h_2h_3 - 2n_e\sum_\alpha\frac{m_e\nu_{e,\alpha}}{m_\alpha+m_e}(T_e-T_i) + \frac{2}{3}n_e\sum_\alpha\frac{m_e m_\alpha\nu_{e,\alpha}}{m_e+m_\alpha}\left[(u_{e,1}-u_{\alpha,1})^2 + u^2_{\alpha,2} + (u_{e,3}-u_{\alpha,3})^2\right] + \frac{2}{3}n_e\sum_\beta\frac{m_e m_\beta\nu_{e,\beta}}{m_e+m_\beta}\left(u^2_{e,1}+w^2_2+u^2_{e,3}\right) + \frac{2}{3}\left(Q^{\mathrm{precip}}_e - C_e\right) \tag{15}$$

where

$$[(\mathbf{u}_e\cdot\nabla)\mathbf{u}_e]_1 = \frac{u_{e,1}}{h_1}\frac{\partial u_{e,1}}{\partial\xi_1} - \frac{u^2_{e,3}}{2h_1h_3^2}\frac{\partial h_3^2}{\partial\xi_1}\,,$$

$q_{e,1}$ is the electron heat flow (defined by equations (64), (66), and (67) of S88), Q^{precip}_e describes heating by electron precipitation (see equation (A4)), C_e describes electron cooling due to excitation of vibrational and rotational levels of N_2 and O_2 [S88, equations (69)–(72)], and excitation of fine structure of *O* [*Williams and McDonald*, 1987, equation (15)].

3. Ion Upflows Caused by Electron Precipitation

[20] All simulations discussed in the present paper start with a quasi-stationary initial state calculated as described in Appendix D. Parameters of the numerical grid are described in Appendix C. Note that in the quasi-stationary state, the parallel flow velocity of O^+ ions is small but finite and it slowly changes with time. Below, the term "upflow" is applied only for parallel ion flows with velocities significantly exceeding the quasi-stationary values.

[21] For simulations with electron precipitation, two values of the precipitation energy are selected: 100 eV and 3.2 keV. In the lower energy case, the ionization and the heating of ambient electrons are maximal at an altitude of about 283 km (see dashed blue curves in Figure 2). In case of higher energy precipitation, electrons penetrate much deeper into the ionosphere, and the ionization and the heating are maximal at an altitude of 124 km (see solid red curves in Figure 2). The time of the simulation (1 January 2007, see Appendix D) corresponds to a minimum in solar activity for which the density of neutrals decays with altitude faster than when the Sun's activity is at its maximum. This allows deeper penetration of precipitating electrons and shifts the ionization and heating area toward lower altitudes. External Alfvén waves are not included. Simulation with Alfvén waves included are analyzed in section 4 without including the electron precipitation effects described here.

[22] The transverse profile of the intensity of electron precipitation is bell-shaped (see Figure 3a), with a transverse scale of about 5 km at the top boundary ($\xi_{1,\min}$). In both the low-energy and high-energy cases, the maximal energy flux of precipitating electrons at the top boundary is 10 erg cm^{-2}s^{-1}. The intensity of the precipitation grows gradually from zero to maximum during a half-a-second interval at the very beginning of the simulation, and then, it remains constant (see Figure 3b). It is necessary to mention that the present model does not account for the scaling of the precipitation energy flux with altitude due to convergence of the geomagnetic field. The error introduced by the lack of this scaling should not be very large because the main simulation area ($\xi_{1,\min} < \xi_1 < \xi_{1,\max}$, see Figure 1) is relatively thin, about 1500 km, so that the difference between cross sections of a flux tube at the top and at the bottom boundaries is small.

[23] For discussions of the importance of different heating and cooling effects below, it is useful to represent equation (15) in the following form

$$\frac{\partial}{\partial t}p_e = Q_{e,u} + Q_{e,p} + Q_{e,q} + Q_{e,i} + Q_{e,E} + Q_{e,pr} + Q_{e,n}\,, \tag{16}$$

where $Q_{e,u}$ assembles all terms proportional to $\mathbf{u}_e\cdot\nabla p_e$, $Q_{e,p}$ assembles all terms proportional to $p_e\nabla\cdot\mathbf{u}_e$, $Q_{e,q}$ contains divergence of the thermal conductivity part of the electron heat flow, $Q_{e,i}$ describes heat exchange with ions, $Q_{e,E}$ assembles all terms describing frictional heating, $Q_{e,pr} = (2/3)Q^{\mathrm{precip}}_e$ describes heating by the precipitation, and $Q_{e,n} = -(2/3)C_e$ describes cooling due to heat exchange with neutrals. Note that both $Q_{e,u}$ and $Q_{e,p}$ contain contributions from the thermoelectric part of the electron heat flow, see equation (64) in S88 and the supplementary information to SR12. Terms $Q_{e,u}$ and $Q_{e,p}$ are referred to as the convection

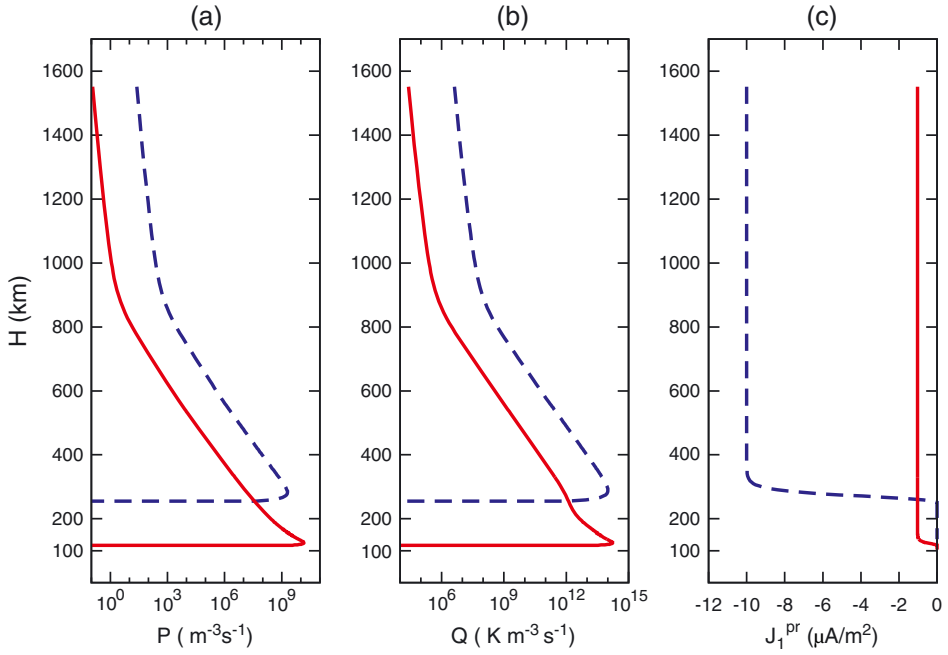

Figure 2. (a) Ionization rate, (b) ambient electron heating rate, and (c) parallel electric current of electron precipitation as functions of altitude. The energy flux of monoenergetic precipitating electrons above the ionosphere is 10 erg $cm^{-2}s^{-1}$, the initial electron energy is 3.2 keV (solid red curves) and 100 eV (dashed blue curves). The profiles are obtained along the center of the precipitation channel where the precipitation intensity is maximal.

and the compression (or rarefaction, depending on the sign of $\nabla \cdot \mathbf{u}_e$) terms, respectively.

3.1. Low-Energy Precipitation

[24] Here the results obtained from simulations corresponding to low-energy precipitation are described. With 100 eV electron precipitation, intense ionization is observed at altitudes from 260 to 400 km (see Figure 4a). A notable feature revealed in the simulation is that the hot plasma column stretches in altitude far beyond the area of intense ionization (see Figure 4b). Direct heating by electron precipitation is found to be significant between 260 and 400 km (see the $Q_{e,pr}$ curve in Figure 5a). Above 400 km, most of the heating is due to the convection $Q_{e,u}$ (see Figure 5b). The thermal conductivity is the major heating source below 270 km and a noticeable heating source above 580 km; between these altitudes, it provides intense cooling (see the $Q_{e,q}$ curve in Figures 5a and 5b). Thus, the thermal conductivity is a very important effect which removes excessive heat from the ionization area and transfers it to both lower and higher altitudes.

[25] Temperature growth saturates once heating is balanced by cooling. Above 260 km, significant cooling is provided by the rarefaction term $Q_{e,p}$ (see the $Q_{e,p}$ curve in Figures 5a and 5b). Below 300 km, inelastic collisions with neutrals are a strong cooling process (see the $Q_{e,n}$ curve in Figure 5a). Note that since there is no ionization below 260 km, the value of $Q_{e,n}$ here is sensitive to the temperature variation but is not affected by the plasma density growth. This maintains high electron temperatures at relatively low altitudes for long times, which is quite different from what happens in the high-energy precipitation case discussed in section 3.2.

[26] The intense ionization and heating associated with low-energy precipitation amplify the electron pressure gradient, which creates a strong upward parallel electric field inside the precipitation channel above the altitude of

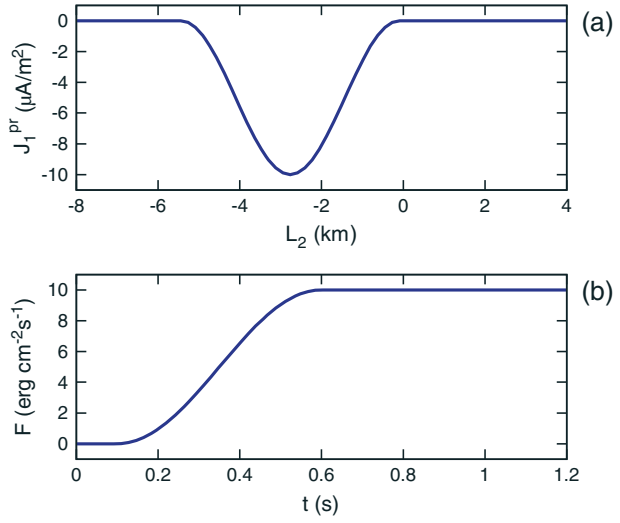

Figure 3. (a) Transverse profile of the parallel electric current of precipitating electrons at altitude about 543 km, the horizontal axis is the distance across the geomagnetic field calculated southward from the middle field line of the simulated area, positive direction of the horizontal axis is southward. The energy flux of electron precipitation in the maximum is 10 erg $cm^{-2}s^{-1}$, the initial electron energy is 100 eV. (b) Temporal dependence of the energy flux of electron precipitation at the initial stage, the flux remains constant for $t > 0.6$ s.

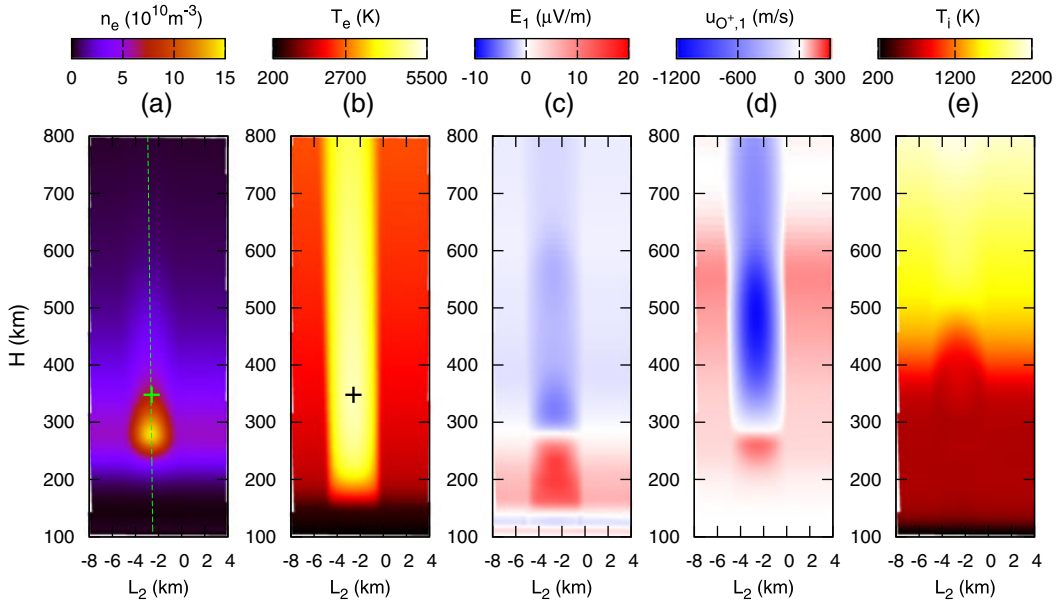

Figure 4. Precipitation of 100 eV electrons. Color maps of the (a) electron density, (b) electron temperature, (c) parallel electric field, (d) parallel O^+ ion flow velocity, and (e) ion temperature at t = 89.68 s. The horizontal axis is the distance across the geomagnetic field, the positive direction is southward. The vertical axis is the altitude. In Figures 4c and 4d, positive values are directed downward. The dashed green line in Figure 4a marks the field line where profiles shown in Figures 5a and 5b are obtained. The cross in Figures 4a and 4b marks position of the probe where time dependencies shown in Figures 8a and 8b are obtained.

maximal ionization (see Figure 4c). This electric field gradually accelerates O^+ ions, and after 90 s, the upflow velocity reaches 1100 m/s at an altitude of 500 km (see Figure 4d and the solid red curve in Figure 6). Although this velocity is a little high, it is not unrealistic. For example, *Wahlund et al.* [1992] observed ion upflows with velocities about 500 m/s at altitudes between 600 and 900 km. The upflow speed in the simulation may be enhanced due to the use of monoenergetic electron precipitation with the energy deposition area localized in a narrow altitude range. Also, the simulation

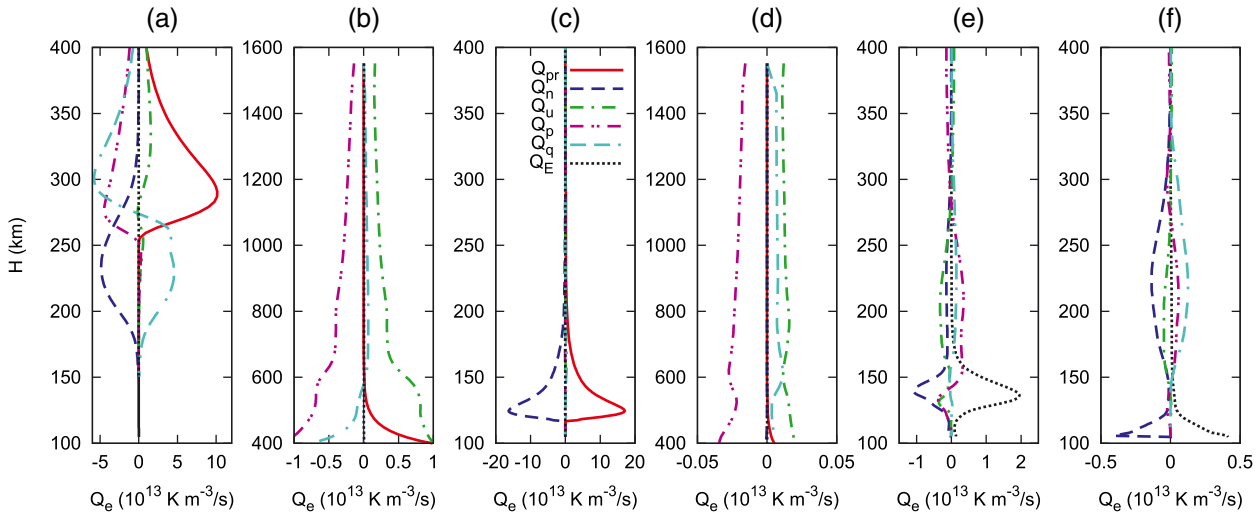

Figure 5. Profiles of rates of electron heating by precipitation $Q_{e,pr}$ (solid red), cooling due to inelastic collisions with neutrals $Q_{e,n}$ (dashed blue), convection energy rate $Q_{e,u}$ (dash-dotted green), compression/rarefaction energy rate $Q_{e,p}$ (dashed double dotted magenta), electron thermal conductivity energy rate $Q_{e,q}$ (double dashed dotted cyan), and frictional heating $Q_{e,E}$ (dotted black). The vertical axis is the altitude. (a, b) For the 100 eV precipitation. (c, d) For the 3.2 keV precipitation. (e, f) For the Alfvén wave with 1 s period. Profiles in Figures 5a–5d are obtained at t = 89.68 s along the center of the electron precipitation channel shown by the dashed green line in Figures 4a and 7e, respectively. Profiles in Figures 5e and 5f are obtained at t = 19.45 s along field lines A and B in Figure 10, respectively.

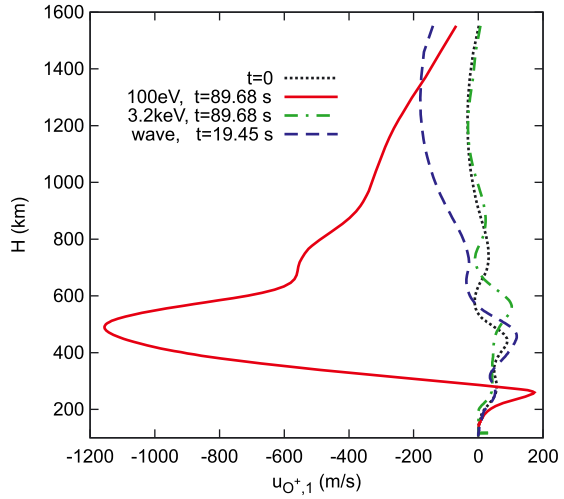

Figure 6. Profiles of the parallel O^+ ion flow velocity at the end of simulations with precipitation of 100 eV electrons (solid red), precipitation of 3.2 keV electrons (dash-dotted green), and Alfvén wave with 1 s period (dashed blue). The vertical axis is the altitude, positive values are directed downward. The profiles for simulations with the 100 eV and 3.2 keV precipitation are obtained at t = 89.68 s along the green dashed line shown in Figures 4a and 7e, respectively. For the simulation with the wave, the profile is obtained along line B in Figure 10a. The dotted black curve shows the initial ion velocity profile.

conditions correspond to solar minimum, and the higher upflow speeds are typical for periods of low Sun activity [*Ogawa et al.*, 2010]. It is interesting that despite the high electron temperature, the ion temperature barely changes (see Figure 4e). In fact, at altitudes between 300 and 500 km, the ion temperature slightly decreases because of the diverging ion flow with $\nabla \cdot \mathbf{u}_{O^+} > 0$ (see the first term in the RHS of equation (9)).

3.2. High-Energy Precipitation

[27] Ionization by 3.2 keV electrons occurs mostly below 200 km. During the 90 s of simulation, the density of plasma in this area gradually grows and reaches very large values (see the density evolution in Figures 7a, 7c, 7e, and 8c). The electron heating, however, is not so effective. The electron temperature rapidly and substantially increases during the first moments of the precipitation (see Figure 7b and the insert in Figure 8d). Then it begins to decrease, showing signs of intense cooling from the bottom layer of the ionosphere (see Figures 7d and 8d). Eventually, the electron temperature acquires a profile close to the initial temperature (see Figure 7f).

[28] Intense electron cooling occurs via inelastic collisions with neutrals. In the present simulation, this cooling along with precipitation heating are the major processes acting below 200 km. Generally, it is expected that there will be a good balance between the related terms in the pressure equation, $Q_{e,n} \approx -Q_{e,pr}$ (see Figure 5c). Term $Q_{e,n}$ is proportional to the plasma density, which grows as shown in Figure 8c. Term $Q_{e,pr}$ is proportional to the precipitation energy flux, which stays constant for $t > 0.6$ s (see Figure 3b). In order to maintain the balance, the electron temperature decreases when the plasma density grows due to ionization. By the end of the simulation, at t = 90 s, the ionization in the lower ionosphere is balanced by recombination and the density growth saturates (see Figure 8c). At

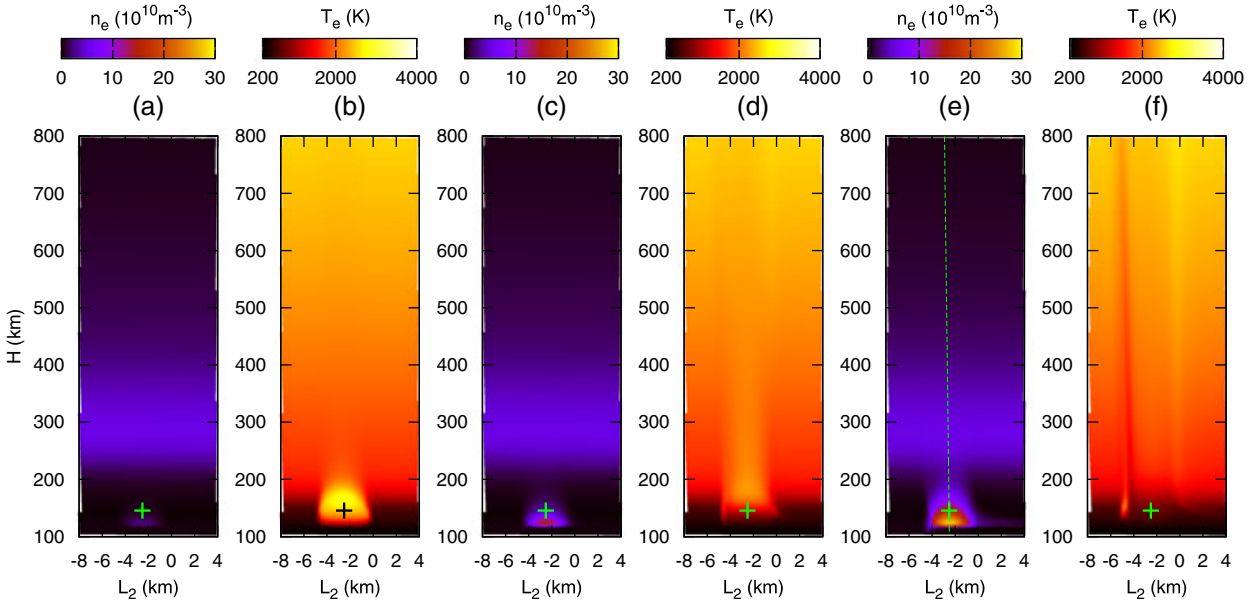

Figure 7. Precipitation of 3.2 keV electrons. Color maps of (a, c, and e) electron density and (b, d, and f) electron temperature. Figures 7a and 7b are obtained at t = 1.99 s. Figures 7c and 7d are obtained at t = 11.96 s. Figures 7e and 7f are obtained at t = 89.68 s. The horizontal axis is the distance across the geomagnetic field, the positive direction is southward. The vertical axis is the altitude. The cross marks the position of a probe where time dependencies shown in Figures 8c and 8d are obtained. The dashed green line in Figure 7e marks the field line where profiles shown in Figures 5c and 5d are obtained.

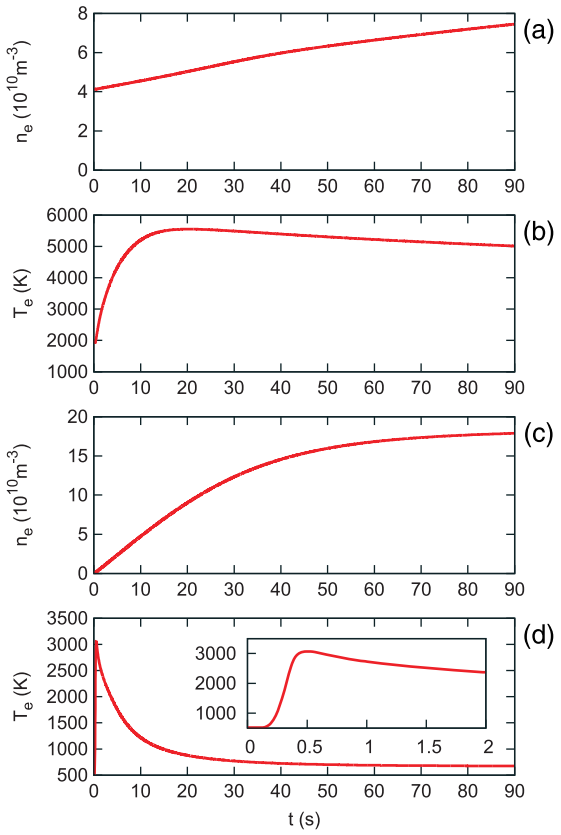

Figure 8. Time dependencies of (a) electron density and (b) temperature for 100 eV electron precipitation in a probe marked by a cross in Figure 4. Time dependencies of (c) electron density and (d) temperature for 3.2 keV electron precipitation in a probe marked by a cross in Figure 7. The insert in Figure 8d shows time dependence of the electron temperature in the probe during the first 2 s.

this stage, the decay of the electron temperature saturates as well (see Figure 8d).

[29] Similar features in the evolution of the electron density and temperature can be found in the simulation with low-energy precipitation discussed in section 3.1. In that simulation, the plasma density grows in the ionization area (see Figure 8a), while the electron temperature reaches a maximum and then decays (see Figure 8b). The evolution of the temperature, however, occurs much more slowly than in the high-energy precipitation case because the cooling due to collisions with neutrals, which strongly depends on the electron temperature, is small in the ionization area (compare solid dashed curves of $Q_{e,n}$ in Figures 5a and 5c). This provides enough time for developing fast O^+ upflows by low-energy electron precipitation.

[30] In the high-energy precipitation case, the initial strong electron temperature perturbation rapidly vanishes, the electron temperature becomes only weakly perturbed compared to the background plasma, the parallel electric field above 200 km is not amplified, and no significant field-aligned ion flow is created (compare the final (dash-dotted green curve) and the initial (dotted black curve) O^+ velocity profiles in Figure 6].

[31] It is necessary to mention that perturbations of electron temperature visible in Figure 7f at $L_2 \approx -5$ km and $L_2 \approx 0$ km are related to field-aligned currents along the edges of the precipitation channel. These currents close the transverse current in the *E*-layer that is enhanced by ionization inside the precipitation channel. This is an example of excitation of an Alfvén wave by electron precipitation.

4. Ion Upflow Caused by a Standing Alfvén Wave in Ionospheric Alfvén Resonator

[32] This section focuses on the response of the ionosphere to Alfvén waves propagation along geomagnetic field lines. The electron precipitation is turned off, and the parallel current J_1 is created by the wave-induced motion of ionospheric electrons and ions only. A simulation is considered in which a wave with a period of 1 s and a transverse electric field amplitude of 1 mV/m is injected at the equatorial plane boundary of the wave transport buffer (see Figure 1). The wave travels through the wave transport buffer for about 16.9 s before entering the main simulation area. The wave amplitude has a bell-shaped profile in the transverse

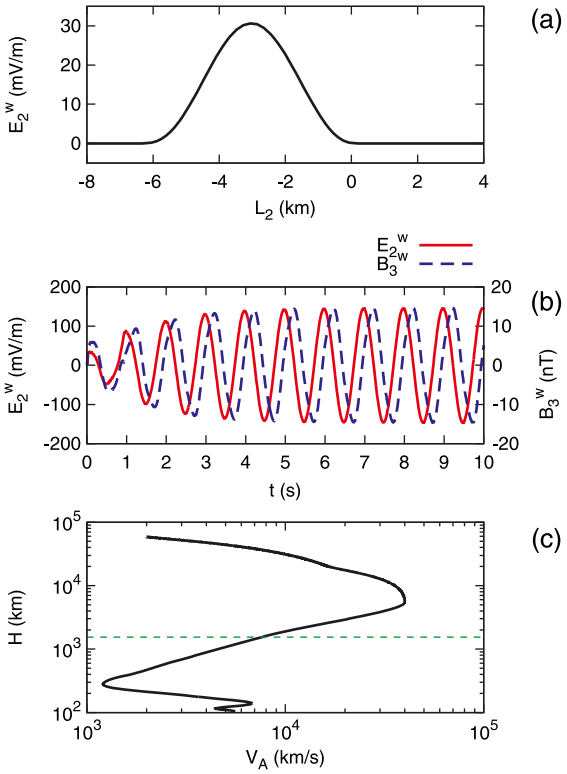

Figure 9. Alfvén wave with 1 s period. (a) Transverse profile of wave electric field at $t = 148$ ms, altitude 1170 km; position of the profile is marked by the horizontal dashed line in Figure 10a. (b) Wave transverse electric field (solid red curve, left vertical axis) and magnetic field (dashed blue curve, right vertical axis) versus time in probe 1 marked by a cross in Figure 10a. (c) Altitude profile of the Alfvén speed along the midplane geomagnetic field line of the system. In Figure 9c, the vertical axis is the altitude, the horizontal green line separates the main simulation area (below the line) and the wave transport buffer (above the line).

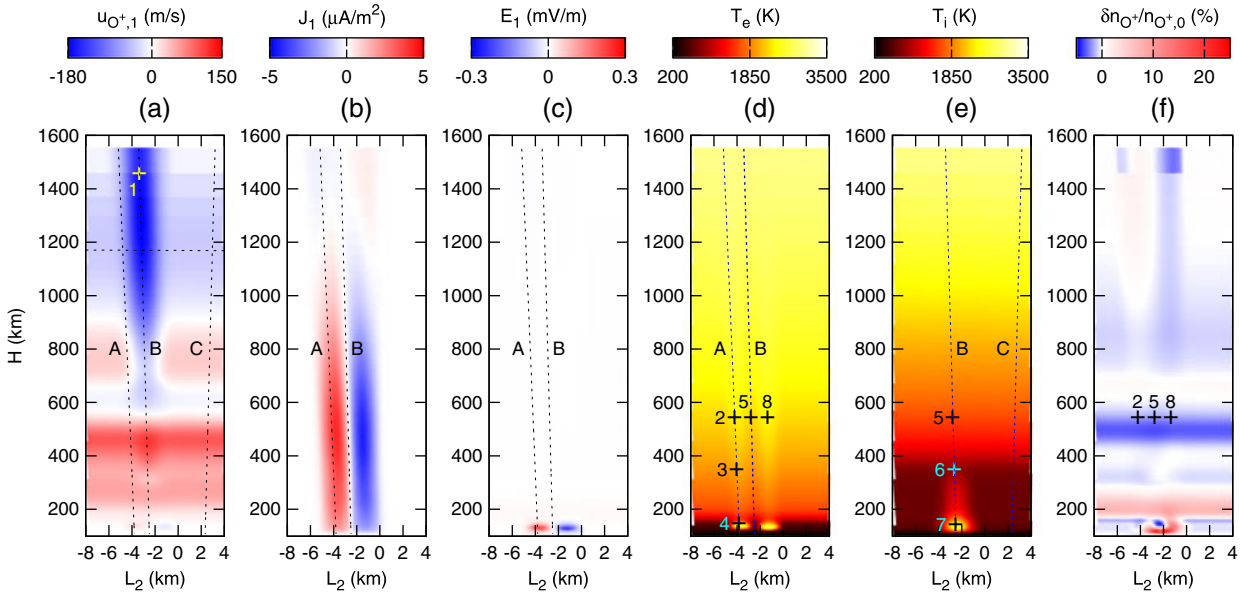

Figure 10. Alfvén wave with 1 s period. Color maps of (a) parallel O^+ ion flow velocity, (b) parallel electric current, (c) parallel electric field, (d) electron temperature, (e) ion temperature, and (f) relative variation of the O^+ density taken at time t = 19.45 s. The horizontal axis is the distance across the geomagnetic field, the positive direction is southward. The vertical axis is the altitude. In Figure 10a, the horizontal dashed line marks the position of the transverse profile shown in Figure 9a. Vertical dashed lines A, B, and C show field lines where the wave has the strongest parallel current (A) and the strongest transverse field amplitude (B), and the field line in the area unaffected by the wave (C). Crosses 1 to 8 mark positions of probes where time dependencies shown in Figures 9b and 11 are obtained. In Figures 10a–10c, positive values are directed downward.

direction with a width of 294 km at the equatorial plane (30 numerical grid cells). At the top of the main simulation area, the width of the amplitude profile is about 6 km (see Figure 9a). Due to convergence of the geomagnetic field, the amplitude of the wave front here is about 30 mV/m. The amplitude of oscillations grows for about 5 s and saturates at 150 mV/m (see Figure 9b). The growth is caused by accumulation of wave energy in the ionospheric Alfvén resonator (IAR). Note that although the main simulation area ends at 1550 km altitude, the IAR is included in the model because the Alfvén speed in the wave transport buffer is nonuniform and has a maximum of 40, 000 km/s at an altitude of 5474 km (see Figure 9c).

[33] By the end of the simulation, a noticeable O^+ upflow area is formed above 600 km, with maximal upflow speed of about 180 m/s near 1300 km altitude (see the dashed blue curve of the 1-D velocity profile in Figure 6, the 2-D color map of the velocity in Figure 10a, and the time dependence of the velocity at a high-altitude probe in Figure 11a).

[34] There are a number of terms in the RHS of the ion motion equation (5). In order to understand the importance of these terms in the formation of the upflow by the wave, it is necessary to consider their values averaged over the wave period. Moreover, since the initial state is not exactly stationary and parallel ion flows gradually develop in the background plasma without any external perturbation, it is necessary to distinguish the background change from the wave effect. To do this, one can compare the averaged terms inside the wave channel (solid red curves in Figure 12) with the corresponding terms at the periphery of the system where the wave is absent (dashed blue curves in Figure 12).

[35] Compared to the background, the wave introduces substantial upward acceleration above 600 km (see Figure 12a). This acceleration is mostly due to the nonlinear Lorentz force $eu_{\alpha,2}B_3$ (see Figure 12b) and the convective velocity derivative term $-[(\mathbf{u}_\alpha \cdot \nabla)\mathbf{u}_\alpha]_1$ (see Figure 12c). The period-averaged Lorentz force $< eu_{\alpha,2}B_3 >$ is the ponderomotive force. The ponderomotive effect requires the gradient of the wave amplitude in the direction of wave propagation, which occurs, e.g., in a standing wave.

4.1. Nonlinear Lorentz Force (The Ponderomotive Effect)

[36] In this simulation, the frequency of the wave is close to the frequency of an IAR harmonic and a standing wave is excited. There is a node of the transverse electric field and an antinode of the azimuthal magnetic field at an altitude of about 550 km (see Figure 13a). The phase shift between the transverse electric and magnetic fields is close to plus or minus 90° depending on altitude (see the solid red curve in Figure 13c and compare the electric and the magnetic field curves in Figure 9b). The wave transverse electric current has a node around 550 km (see Figure 13b). The current amplitude is very strong around 300 km, where the plasma density is maximal. The spike at 120 km is due to the intense Pedersen current in the *E*-layer.

[37] The phase shift between the transverse electric current and the magnetic field is close to –180° above 600 km; below 400 km, the phase shift is close to zero almost

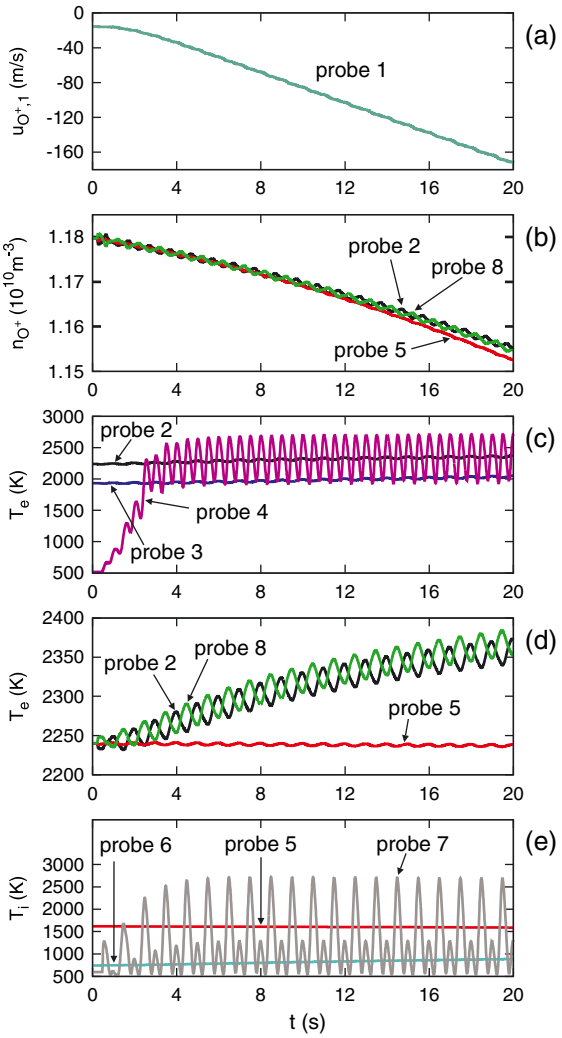

Figure 11. Alfvén wave with 1 s period. Time dependencies of the following values. (a) Parallel O^+ velocity in probe 1. (b) Density of O^+ ions in probes 2, 5, and 8. (c) Electron temperature in probes 2, 3, and 4. (d) Electron temperature in probes 2, 5, and 8. (e) Ion temperature in probes 5, 6, and 7. The probe positions are shown in Figure 10.

everywhere except near 200 km (see the dashed blue curve in Figure 13c). The ponderomotive force is negative and accelerates ions upward above 550 km; below this altitude, the force is positive and directed downward (see the solid red curve in Figure 12b). This force is not observed in areas where the wave is not present (see the dashed blue curve in Figure 12b), so it cannot be attributed to the gradually changing background electromagnetic field.

[38] The ratio of the Alfvénic ($\propto \partial E_2/\partial t$) and Pedersen ($\propto E_2$) parts of the transverse electric current is of the order of the ratio of the wave frequency ω and the ion-neutral collision frequency (see equation (6)). This ratio becomes close to unity near 180 km altitude (compare the solid red curve of ν_{O^+} with the short-dashed green line of ω in Figure 13d). The transverse current is mostly Alfvénic above this altitude and mostly Pedersen below. Note that the phase shift between the transverse current and the magnetic field grows as one descends from 300 to 200 km but it decreases again below 200 km (see the dashed blue curve in Figure 13c). The decrease occurs due to the transition to the Pedersen mode of the transverse current. This, in particular, keeps the ponderomotive force directed downward in the *E*-layer (see the solid red curve in Figure 12b below 200 km).

[39] The ponderomotive effect in IAR was considered previously by *Streltsov and Lotko* [2008] and *Sydorenko et al.* [2008]. Figure 5 of *Streltsov and Lotko* [2008] shows modification of ion density by the ponderomotive force. Although there is no vertical ion flow velocity data, the increase of the density near the low-altitude boundary suggests that the ion flow is directed downward near this boundary. The pattern of the ion flow, which is downward in the lowest plasma layer and upward at higher altitudes, as follows from the results of *Streltsov and Lotko* [2008], qualitatively agrees with the direction of the ponderomotive force in the present simulation (solid red curve in Figure 12b).

[40] The present simulation is focused on forces affecting ion motion rather than density modification. The simulation is relatively short, and it is difficult to notice any substantial plasma density change due to the ponderomotive effect, especially when there are gradual changes in the background plasma density. In fact, in most of the simulation area, except for the lowest plasma layers, the relative variation of the O^+ ion density is only a few percent (see Figure 10f). The diverging velocity pattern (see Figure 10a) suggests that a density cavity should form around the altitude of 600 km. Similar cavities are reported in *Streltsov and Lotko* [2008] and *Sydorenko et al.* [2008]. The beginning of the formation of such a cavity in the present simulation can be noticed if one compares the time evolution of the ion density in three probes positioned at the same altitude ($\approx$ 550 km) at different transverse coordinates (the probes labeled 2, 5, and 8 are shown in Figure 10f). Note that the density in the center of the wave propagation channel (probe 5) decreases slightly faster than the density in probes 2 and 8 (see Figure 11b).

[41] The model of *Streltsov and Lotko* [2008] uses a height-integrated conductivity boundary condition at the low-altitude end and considers collisionless plasma, so the transverse current is purely Alfvénic in the plasma but is Pedersen in the boundary. The model of *Sydorenko et al.* [2008] also considers collisionless plasma but it uses a perfectly conducting surface as the boundary condition at the low-altitude end. As a result of this simplified boundary condition, the electromagnetic field pattern in the simulation of *Sydorenko et al.* [2008] is such that the ponderomotive force near the low-altitude boundary is directed upward [see *Sydorenko et al.*, 2008, Figure 7]. Thus, the imposition of a perfectly conducting layer boundary condition has important consequences for the direction of the ponderomotive force near the boundary.

4.2. Convective Velocity Derivative

[42] The time-averaged velocity convection derivative (10) also reveals upward acceleration above 600 km (see the solid red curve in Figure 12c). Here the fourth and the fifth terms in the RHS of (10) corresponding to centrifugal acceleration are dominant. While the centrifugal acceleration is directed away from the Earth, the average acceleration due to the convection derivative is directed downward at lower altitudes (see the spike below 200 km in solid red curve in Figure 12c). It appears here that a

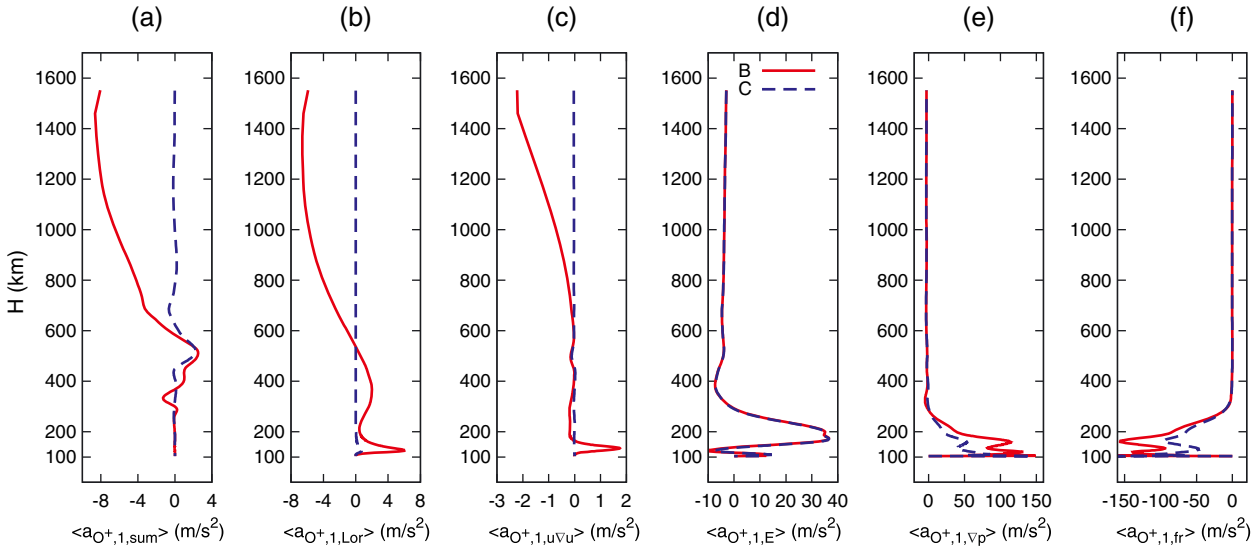

Figure 12. Alfvén wave with 1 s period. Altitude profiles of the following values for O^+ ions averaged over time interval 18.7 s < t < 19.7 s. (a) Full parallel acceleration. (b–f) Contributions to the full parallel acceleration of the Lorentz force (Figure 12b), the convection velocity derivative term (Figure 12c), the parallel electric field (Figure 12d), the O^+ pressure gradient (Figure 12e), and the friction with other species (Figure 12f). Profiles B (solid red) and C (dashed blue) are obtained along the vertical dashed lines B and C in Figure 10, respectively. The vertical axis is the altitude. Positive values are directed downward.

significant downward (positive when in RHS of (5)) contribution comes from the third term in the RHS of (10) proportional to $u_{\alpha,1}u_{\alpha,2}\partial h_1/\partial\xi_2$. This term describes parallel acceleration of a two-dimensional flow due to the curvature of dipole geometry. Acceleration related to the convective velocity derivative is observed only inside the wave channel, and thus, it is not related to slow changes in the background (compare solid red and dashed blue curves in Figure 12c).

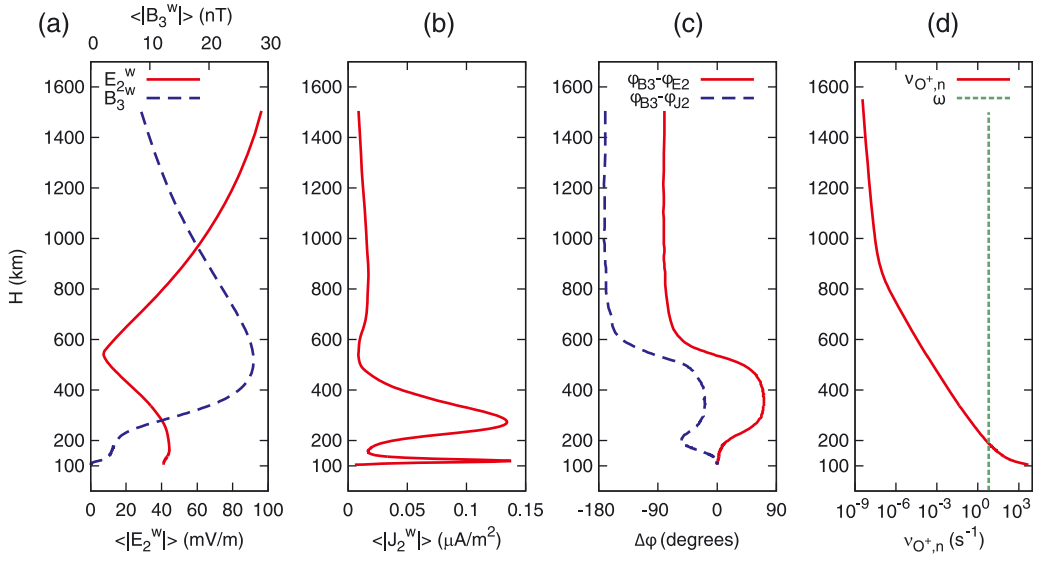

Figure 13. Alfvén wave with 1 s period. Altitude profiles of the following values. (a) Absolute value of wave transverse electric field (solid red curve, bottom horizontal axis) and wave magnetic field (dashed blue curve, top horizontal axis) averaged over a wave period. (b) Absolute value of transverse wave electric current averaged over a wave period. (c) Phase difference between wave transverse magnetic and electric fields (solid red curve) and phase difference between wave transverse magnetic field and electric current (dashed blue curve). (d) Frequency of ion-neutral collisions for O^+ at t = 19.45 s (solid red curve) and the wave frequency ω (short-dashed green curve). The averaging and the calculation of the phases is performed over time interval 18.7 s < t < 19.7 s. The profiles are obtained along the center of the wave propagation channel marked by the vertical dashed line B in Figure 10. The vertical axis is the altitude.

4.3. Parallel Electric Field

[43] There are two main sources of intense parallel electric field in the lower ionosphere. One is a strong parallel current flowing through an area with low conductivity. The other is an enhanced electron temperature gradient. The parallel wave current (see Figure 10b) is the strongest along field lines where the transverse gradient of the wave amplitude is maximal (e.g., line A in Figure 10, see also Figure 9a). Without electron precipitation, frictional heating is the major electron heating mechanism. It is the strongest at low altitudes, about 135 km (see the dotted black curve in Figure 5e). In contrast to the simulation with 3.2 keV electron precipitation discussed in section 3.2, there is no accumulation of plasma density due to ionization and cooling due to inelastic collisions with neutrals is not balancing heating completely (see the dashed blue curve in Figure 5e). As a result, there are strong oscillations of the electron temperature at low altitudes (see the electron temperature snapshot in Figure 10d and compare the electron temperature evolution in low-altitude probe 4 with that in high-altitude probes 3 and 2 shown in Figure 11c). This creates a substantial parallel electric field (see Figure 10c), but friction with neutrals at low altitudes is so strong (see section 4.4 below) that parallel ion flows do not develop.

[44] In the center of the wave channel (line B in Figure 10), where the strongest ion upflow is formed at high altitudes, the wave parallel current is minimal. The frictional electron heating (dotted black curve in Figure 5f) and the electron temperature fluctuations are small as well (compare time dependence of the temperature in probe 5 in the center of the wave channel with that in probes 2 and 8 in the intense parallel current areas shown in Figure 11d). The effect of the wave parallel electric field on ion motion barely differs from that in the background plasma (compare solid red and dashed blue curves in Figure 12d).

4.4. Ion Pressure Gradient and Friction With Neutrals

[45] In the present simulation, the ion pressure (Figure 12e) and the friction force (Figure 12f), together with the parallel electric field force discussed above, are the major factors below 300 km. The electric current of the wave heats ions at altitudes below 400 km (the profile of the frictional ion heating $Q_{i,E}$ is shown by a dotted black curve in Figure 14a, see also the ion temperature snapshot in Figure 10e). Note that $Q_{i,E}$ contains the fifth and the sixth terms in the RHS of (9) and combines both the parallel and the transverse ion flow. The contribution of the transverse current, however, is dominant at these altitudes. The frictional heating is largely balanced by heat exchange with neutrals $Q_{i,n}$ (dashed blue curve in Figure 14a), which is described by the third term in the RHS of (9). The sum of $Q_{i,E}$ and $Q_{i,n}$ has a maximum around 225 km (solid red curve in Figure 14b), but the intense ion temperature oscillations are observed at lower altitudes, below 150 km, where the ratio $(Q_{i,E}+Q_{i,n})/n_e$ is higher (compare the solid red curve of $Q_{i,E}+Q_{i,n}$ with the dashed green curve of n_e in Figure 14b, also compare the ion temperature evolution in low-altitude probe 7 with that in probes 6 and 5 at higher altitudes shown in Figure 11e). It is necessary to mention that in the present simulation, the other heating and cooling terms in the RHS of (9) are much smaller than $Q_{i,E}+Q_{i,n}$.

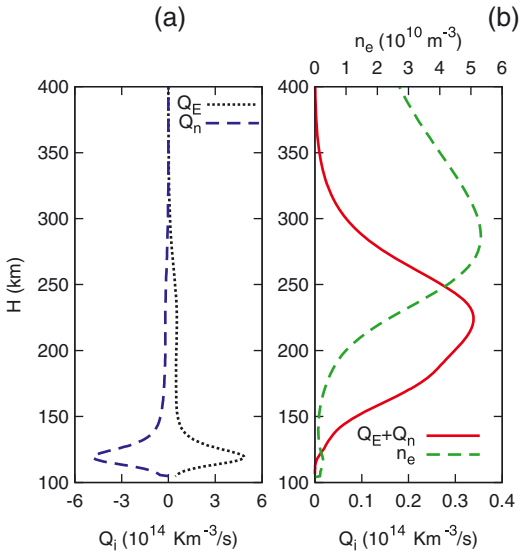

Figure 14. (a) Profiles of rates of ion frictional heating $Q_{i,E}$ (dotted black) and cooling due to heat exchange with neutrals $Q_{i,n}$ (dashed blue). (b) Profiles of the sum of rates $Q_{i,E}+Q_{i,n}$ (solid red, bottom horizontal coordinate axis) and electron density (dashed green, top horizontal coordinate axis). The vertical axis is the altitude. Profiles are obtained at t = 19.45 s along field line B in Figure 10.

[46] The effect of ion heating on the O^+ motion at lower altitudes is somewhat surprising. Although the ion temperature has a peak near 140 km and decreases with altitude up to about 350 km, the average O^+ ion pressure force here is directed downward and not upward (see the solid red curve in Figure 12e below 300 km). The reason is that the O^+ density increases with altitude so rapidly (see Figure D1a) that the ion pressure increases with altitude even though the temperature decreases.

[47] The ion heating by the wave current does not change qualitatively the pattern of the pressure gradient force existing in the background plasma, but rather increases (approximately by a factor of 2) the downward force below 300 km (compare the solid red and the dashed blue curves in Figure 12e). The effect of this force is much larger than the combined ponderomotive effect and the convective velocity derivative (compare Figure 12e with Figures 12b and 12c). The collision frequency below 200 km, however, is high, in the range of 1–10^3 s^{-1} (see the solid red curve in Figure 13d), and acceleration of the ion flow by just a few meters per second is sufficient to amplify the friction force enough to balance this strong additional downward force (compare the solid red and the dashed blue curves in Figure 12f). As a result, the ion heating in the E-layer does not produce significant parallel ion flows.

5. Conclusion

[48] In this paper, a comprehensive model of magnetosphere-ionosphere coupling that accounts for Alfvén wave dynamics and electron precipitation is described. The ionosphere is represented as a layer of collisional plasma that smoothly transitions to the collisionless regime at high altitude. This is an important

advance over other models that represent the ionosphere as a height-integrated conductivity layer of zero thickness. The height-resolved ionosphere used in the present study incorporates important collision and chemical reaction processes following *Schunk* [1988], *Blelly et al.* [1996], *Tian et al.* [2008], and *Williams and McDonald* [1987]. As an example of the effectiveness of the model, simulations of ion upflows induced by soft electron precipitation are described. Although not a fundamentally new topic, the results presented here show quantitatively that low-energy electrons are more effective at creating ion upflow. This is in agreement with the predictions of numerical models of *Liu et al.* [1995], *Su et al.* [1999], *Vontrat-Reberac et al.* [2001], *Lynch et al.* [2007], and *Sadler et al.* [2012].

[49] In the case of 100 eV electron precipitation, ionospheric electrons are heated most efficiently at altitudes ranging between 250 and 400 km, with a maximum around 280 km altitude. It is found that in this case, heat conductivity raises the electron temperature within a much wider range of altitude, from 160 km up to about 1500 km. This amplifies upward-directed parallel electric fields and creates strong O^+ ion upflow above 300 km.

[50] An aspect of simulations presented here is that the electron temperature profile is affected by the boundary condition that requires the electron temperature to remain constant at the topside boundary of the main simulation area (see Appendix B). The electron temperature at the top boundary is a simulation parameter and changing it affects the ion upflow in the following way: In the pressure gradient $\partial(nT)/\partial\xi_1$, the density gradient term $T\partial n/\partial\xi_1$ is usually more important than the temperature gradient term $n\partial T/\partial\xi_1$, which is why higher electron temperature at the topside boundary produces stronger parallel electric fields and higher upflow velocities. This boundary condition is not the only one possible. For comparison, *Rees et al.* [1971] considered the following high-altitude boundary conditions: "zero net heat flux" and "zero conducted heat flux." With the former condition, the electron temperature in the auroral ionosphere was increasing with altitude (though with a variable rate) and the conducted heat flow was directed downward. The latter condition produced results closer to the present model: the temperature profile had a maximum around 400 km and the conducting heat flow was directed upward above (and downward below) this altitude, similar to what is described in section 3.1.

[51] In the second simulation presented, heating of the ionosphere by high-energy (3.2 keV) electron precipitation is found to occur at much lower altitudes than for soft electron precipitation: between 117 and 200 km (with a maximum at 124 km inside the *E*-layer). Ionization in this situation increases the plasma density significantly, while at the same time, electrons are cooled down rapidly by frequent inelastic collisions with neutrals. Without an increase of the electron temperature at low altitudes, heat conductivity is not able to increase the electron temperature (and the parallel electric field, respectively) at high altitudes. This implies there is no enhanced parallel electric field and no ion upflow, and thus, soft electron precipitation is more effective at driving ion upflow. This does not imply, however, that high-energy electron precipitation can never create ion upflows. For example, *Rees et al.* [1971] used energetic precipitation with a rather wide energy spectrum, which led to maximal heating at around 110 km altitude. The precipitation energy flux in *Rees et al.* [1971] was 7.8 times larger than in the present paper. As a result, despite the lower efficiency of ionospheric heating by high-energy electrons, there was an increase of the electron temperature above 400 km, and an upward-directed parallel electric field that reached 1.5 μV/m. Ion upflow is not discussed in *Rees et al.* [1971], but simulations using the present model show that ion upflow is present under similar parallel electric field.

[52] A useful feature of the model presented in this paper is that the boundary condition for the electromagnetic field includes a nonmonotonic Alfvén speed profile that allows study of processes in the ionospheric Alfvén resonator. In a simulation where the ionosphere is driven by an Alfvén wave with a period of 1 s, an eigenmode of the resonator is excited and ion upflow is driven by the ponderomotive (time-averaged nonlinear Lorentz) force similar to *Streltsov and Lotko* [2008] as well as by the centrifugal acceleration similar to *Cladis* [1986]. Note that unlike *Streltsov and Lotko* [2008], the present model does not use height-integrated conductivity and resolves the full dynamics of the *E*-layer plasma. Wave currents flowing through the *E*-layer produce electron and ion heating in this area, but due to strong collisions, the increase of the period-averaged effect of parallel electric field and ion pressure gradient is balanced by the friction force, and the related field-aligned ion flows are insignificant. The efficiency of ion upflow formation by ion heating may improve if the heating is applied for a longer time. This can be achieved, for example, if an Alfvén wave with a larger period is used. The case with a low-frequency Alfvén wave will be discussed in a separate publication.

[53] There are a number of simplifications in the model which limit its applicability. Hall conductivity is omitted although it may exceed the Pedersen conductivity in the *E*-layer. The model does not include He^+ because it uses the model of chemical reactions of *Blelly et al.* [1996] where this element was omitted. He^+, however, is a common polar wind component [*Yau et al.*, 2007]. The vertical component of the neutral wind is omitted as well as the possibility to study the response of the thermosphere on ion upflows. The electron precipitation model assumes monoenergetic electrons at the top boundary, while in reality, there is usually some spread of the energy spectrum. These drawbacks will be eliminated in the future.

Appendix A: Model of Electron Precipitation

[54] It is assumed that the electrons precipitating into the ionosphere are monoenergetic and move parallel to the geomagnetic field at the top boundary of the ionosphere. In this case, the differential electron flux as a function of position along the precipitation path is given by the following formula [*Maeda and Aikin*, 1968; *Rees*, 1969]:

$$j(E,z) = g_0 \exp\left[-4.42\left(\frac{z}{R}\right)^{2.8}\right]\frac{i(E,E_0,z)}{I(E_0,z)},\ [\text{electrons m}^{-2}\text{s}^{-1}\text{eV}^{-1}], \tag{A1}$$

where E is the electron energy,

$$z = \int_0^L \rho\, \mathrm{d}l,\ [\text{g cm}^{-2}]$$

is the atmospheric depth at the observation point (integration is over the distance l along the geomagnetic field, at the top boundary $l = 0$), L is the distance from the top boundary to the observation point, ρ is the atmospheric mass density, g_0 is the initial intensity of the precipitation measured in electrons $m^{-2}s^{-1}$, E_0 is the initial energy of precipitation,

$$R = 4.57 \cdot 10^{-6} E_0^{7/4} , \ [\mathrm{g\ cm^{-2}}] \tag{A2}$$

is the electron range describing the distance an electron with energy E_0 can travel through the air [in (A2), E_0 is in keV],

$$i(E, E_0, z) = \left\{ \frac{1 - E/E_0}{\left[1 - (1 - z/R)^{0.571}\right]^{0.1}} \right\}^a \exp\left(- \left\{ \frac{1 - E/E_0}{\left[1 - (1 - z/R)^{0.571}\right]^{0.9}} \right\}^a \right),$$

$$a = 7.5 \frac{z}{R} + 3.25 ,$$

$$I(E_0, z) = \int_0^{E_0} i(E, E_0, z) \mathrm{d}E .$$

[55] The ionization rate for a process where an ion of species α is produced out of a neutral of species β is calculated as

$$r_{\beta,\alpha}(z) = \int_0^{E_0} j(E, z) \sigma_{i,\beta,\alpha} n_\beta \mathrm{d}E , \tag{A3}$$

where $\sigma_{i,\beta,\alpha}$ is the cross section of the ionization process and n_β is the number density of the neutral species. The present model accounts for the following ionization processes:

$$\begin{aligned}
&\text{(i)}\ \mathrm{O} + e^- \rightarrow \mathrm{O}^+ + 2e^- \\
&\text{(ii)}\ \mathrm{O_2} + e^- \rightarrow \mathrm{O}^+ + \mathrm{O} + 2e^- \\
&\text{(iii)}\ \mathrm{O_2} + e^- \rightarrow \mathrm{O_2^+} + 2e^- \\
&\text{(iv)}\ \mathrm{N_2} + e^- \rightarrow \mathrm{N}^+ + \mathrm{N} + 2e^- \\
&\text{(v)}\ \mathrm{N_2} + e^- \rightarrow \mathrm{N_2^+} + 2e^- .
\end{aligned}$$

Cross sections for process (i) are from Table 12 of *Majeed and Strickland* [1997]; for processes (ii) and (iii), they are taken from Table 11 of *Itikawa* [2009]; for processes (iv) and (v), they are taken from Tables 15 to 17 of *Itikawa* [2006].

[56] The rate of ambient electron gas heating due to electron precipitation is

$$Q_e^{\mathrm{precip}} = \int_0^{E_0} \mathrm{d}E j(E, z) \sum_\beta n_\beta \int_0^{E - W_{i,\beta}} \mathrm{d}E_s E_s \frac{\left|\frac{\mathrm{d}E}{\mathrm{d}x}\right|_e}{\left|\frac{\mathrm{d}E}{\mathrm{d}x}\right|_e + \left|\frac{\mathrm{d}E}{\mathrm{d}x}\right|_n} S_\beta(E, E_s) , \tag{A4}$$

where $W_{i,\beta}$ is the ionization energy threshold for neutral species β ($\beta = \mathrm{O}, \mathrm{O_2}, \mathrm{N_2}$), E_s is the secondary electron energy (a secondary electron is an electron extracted from the atom in an ionization event),

$$\left|\frac{\mathrm{d}E}{\mathrm{d}x}\right|_e = \frac{1.95 \cdot 10^{-12} n_e}{E} , \ [\mathrm{eV\ cm^{-1}}]$$

is the secondary electron energy loss rate due to collisions with ambient electron gas [*Rees et al.*, 1969] with electron energy E in eV,

$$\left|\frac{\mathrm{d}E}{\mathrm{d}x}\right|_n = \sum_\beta n_\beta \sum_k \Delta W_{\beta,k} \sigma_{\beta,k} , \ [\mathrm{eV\ cm^{-1}}] \tag{A5}$$

is the rate of secondary electron energy loss due to inelastic collisions with neutral atoms and molecules [*Rees et al.*, 1969], $\Delta W_{\beta,k}$ and $\sigma_{\beta,k}$ are the energy threshold and cross section of inelastic collision process k for neutral species β,

$$S_\beta(E_p, E_s) = \sigma_{i,\beta} \frac{G(E_p, E_s, W_{i,\beta})}{N_\beta(E_p)}$$

is the differential ionization cross section for neutral species β, $\sigma_{i,\beta}$ is the total ionization cross section for neutral species β, E_p is the energy of the primary (precipitating) electron,

$$G(E_p, E_s, W_{i,\beta}) = \exp\left[-\frac{E_s + W_{i,\beta}}{31.5} - 339 \exp\left(-\frac{E_s + W_{i,\beta}}{2.49} \right) \right] \times \frac{1}{E_s + W_{i,\beta}} \ln\left(\frac{\sqrt{E_p} + \sqrt{E_p - W_{i,\beta} - E_s}}{\sqrt{E_p} - \sqrt{E_p - W_{i,\beta} - E_s}} \right)$$

is the shape function defined by *Rees et al.* [1969], and

$$N_\beta(E_p) = \int_0^{E_p - W_{i,\beta}} \mathrm{d}E_s G(E_p, E_s, W_{i,\beta}) .$$

The total ionization cross sections for O, N_2, and O_2 are from the same sources as the cross sections for ionization processes (i)–(v) above. The ionization thresholds are $W_{i,O} = 13.6$ eV, $W_{i,N_2} = 15.6$ eV, and $W_{i,O_2} = 12.1$ eV [*Rees et al.*, 1969; *Majeed and Strickland*, 1997]. Inelastic cross sections $\sigma_{\beta,k}$ and energy thresholds $\Delta W_{\beta,k}$ used in (A5) are listed in Tables 4 to 14 of *Majeed and Strickland* [1997].

[57] Note that the differential electron flux (A1) conceals information about the distribution of scattered precipitating electrons over pitch angle ϑ because it is obtained as

$$j(E, z) = \int f(E, \cos\vartheta, z) \mathrm{d}\cos\vartheta ,$$

where $f(E, \cos\vartheta, z)$ is the distribution function of precipitating electrons. The parallel electric current of precipitating electrons is

$$J_{1,\mathrm{precip}}(z) = -e \int f(E, \cos\vartheta, z) \cos\vartheta \mathrm{d}\cos\vartheta \mathrm{d}E \neq -e \int j(E, z) \cos\vartheta \mathrm{d}\cos\vartheta \mathrm{d}E .$$

Unfortunately, the analytical expression for the distribution function $f(E, \cos\vartheta, z)$ is difficult to find in the literature. However, the angular dependence can be accounted for if $f(E, \cos\vartheta, z) = f_E(E, z) f_\vartheta(\vartheta, z)$. In this case, the parallel energy flux G_1 is

$$G_1 = \int f(E, \cos\vartheta, z) E \cos\vartheta \mathrm{d}\cos\vartheta \mathrm{d}E = \int j(E, z) E \mathrm{d}E \frac{\int f_\vartheta \cos\vartheta \mathrm{d}\cos\vartheta}{\int f_\vartheta \mathrm{d}\cos\vartheta} .$$

If one omits possible dependence of f_ϑ on the parallel distance l, then

$$\frac{\frac{\partial}{\partial l} G_1}{\frac{\partial}{\partial l} \int j(E, z) E \mathrm{d}E} = \frac{\int f_\vartheta \cos\vartheta \mathrm{d}\cos\vartheta}{\int f_\vartheta \mathrm{d}\cos\vartheta} \equiv \epsilon . \tag{A6}$$

The divergence of the parallel energy flux must be equal to the total energy loss rate of precipitating electrons

$$\frac{\partial}{\partial l} G_1 = \int_0^{E_0} \mathrm{d}E j(E,z) \sum_\beta n_\beta \int_0^{E-W_{\beta,i}} \mathrm{d}E_s E_s S_\beta(E,E_s) + \sum_\beta r_\beta W_{i,\beta} \,, \tag{A7}$$

where the first term in the RHS describes the energy transferred to the secondary electrons (compare with (A4)), and the second term describes ionization losses, $r_\beta = \sum_\alpha r_{\beta,\alpha}$ is the total ionization rate for neutral species β. Using (A7), the ratio in the left-hand side of (A6) can be calculated numerically. For example, for 3.2 keV precipitation and the atmosphere considered in the present paper, this ratio varies from $\frac{1}{3}$ to $\frac{1}{5} \ll 1$ along the precipitation path. Note that $\int_0^1 f_\vartheta \cos\vartheta \,\mathrm{d}\cos\vartheta \ll \int_0^1 f_\vartheta \,\mathrm{d}\cos\vartheta$ if function f_ϑ is maximal near $\vartheta = \pi/2$. This creates a conflict with *Maeda* [1965], who shows that the angular distribution of precipitating electrons approaches $\cos^2\vartheta$ shape. One explanation of this discrepancy is that the differential electron flux given by formula (A1) decays too fast, which increases the denominator in the left-hand side of (A6). This assumption is supported by Figure 4 of *Maeda and Aikin* [1968], where the distribution given by the formula is about 2 times lower than the distribution obtained in Monte Carlo simulation (compare curves labeled $\xi = 0.9$ in that figure). Technically, the rate of decay of the differential electron flux (A1) can be reduced if the electron range R increases compared to the value defined by equation (A2). In the present paper, however, the range R is not modified and the parallel electric current of precipitating electrons is calculated as

$$J_1(z) = -e \int j(E,z)\mathrm{d}E \frac{\int f_\vartheta \cos\vartheta \,\mathrm{d}\cos\vartheta}{\int f_\vartheta \,\mathrm{d}\cos\vartheta} = -\epsilon e \int j(E,z)\mathrm{d}E \,,$$

where factor ϵ is the angular term calculated according to (A6). For 100 eV and 3.2 keV precipitation energies, the angular term is $\epsilon = 0.1$ and $\epsilon = \frac{1}{3}$, respectively.

Appendix B: Boundary Conditions

[58] The present model uses the same boundary conditions at the bottom boundary of the main simulation area ($\xi_1 = \xi_{1,\max}$, see Figure 1) as the model of SR12. The electromagnetic field boundary conditions at the interface between the main simulation area and the wave transport buffer ($\xi_1 = \xi_{1,\min}$) are also same as in SR12. A new condition introduced here is that both electron and ion temperatures are constant. The advection equations are solved using a semi-Lagrangian method [*Staniforth and Côté*, 1991] which is quite "undemanding" with respect to boundary conditions. If ions flow upward at $\xi_1 = \xi_{1,\min}$, the ion continuity equation (8) does not require any boundary conditions. In case of ion inflow, however, some assumption must be made about the ion density profile beyond the boundary. A simple approach which gives reasonable results is to omit field-aligned convection $[(u_{\alpha,1}/h_1)\partial n_\alpha/\partial\xi_1$ term in (8)] at $\xi_1 = \xi_{1,\min}$ if an ion inflow is detected there. This is equivalent to a uniform ion density along the geomagnetic field beyond the boundary, $\partial n_\alpha/\partial\xi_1 = 0$.

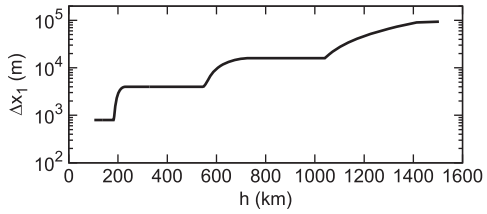

Figure C1. Variation of the size of the grid cell along the geomagnetic field with altitude.

[59] Boundary conditions at the northern ($\xi_2 = \xi_{2,\min}$) and southern ($\xi_2 = \xi_{2,\max}$) boundaries are as follows:

$$\begin{aligned} E_1(\xi_1,\xi_{2;\min,\max},t) &= -\frac{1}{en_e h_1}\frac{\partial}{\partial\xi_1} p_e(\xi_1,\xi_{2;\min,\max},t) \,, \\ \frac{\partial}{\partial\xi_2} n_\alpha(\xi_1,\xi_{2;\min,\max},t) &= 0 \,, \\ \frac{\partial}{\partial\xi_2} p_\gamma(\xi_1,\xi_{2;\min,\max},t) &= 0 \,, \\ n_\alpha(\xi_1,\xi_{2,\min},t) &= n_\alpha(\xi_1,\xi_{2,\max},t) \,, \\ p_\gamma(\xi_1,\xi_{2,\min},t) &= p_\gamma(\xi_1,\xi_{2,\max},t) \,. \end{aligned} \tag{B1}$$

Unlike the boundary conditions used in SR12, conditions (B1) permit time variation of ion densities, which prevents formation of density jumps near the boundary geomagnetic field lines when the chemistry and the field-aligned ion flows are included. Since conditions (B1) are essentially periodic while the dipole geomagnetic field is not, in simulations with transversely localized external drivers (such as Alfvén waves or electron precipitation), a limitation is imposed similar to SR12: the simulation must be stopped when a perturbation created by the external driver reaches the boundary.

Appendix C: Numerical Grid Parameters

[60] The model uses rectangular structured nonuniform numerical grid in dipole coordinates similar to the one described in SR12. The grid has a central area with high uniform transverse resolution and two side buffer areas where the resolution gradually reduces toward the boundaries. The role of the buffer areas is discussed in SR12. The central area has the following parameters. The northern bottom corner is at magnetic latitude 71.64° and altitude 105 km. The northern top corner is at altitude 1553 km. There is 90 cells in the transverse direction and 248 cells in the parallel direction. Transverse size of the grid cell is 161 m at the bottom, and it linearly grows with altitude up to 218 m at the top. The parallel size of the grid cell at the bottom is 796.5 m, it increases with altitude as shown in Figure C1. At the top of the main simulation area, the parallel size of the grid cell is 93, 567 m. A significant increase of the parallel cell size near the top boundary (above 1050 km in Figure C1) has been introduced to mitigate a numerical effect of excitation of ion density waves at the top boundary. The time step in the simulation is $\Delta t = 9.1417 \cdot 10^{-4}$ s.

Appendix D: Calculation of a Quasi-Stationary State for Initial Conditions

[61] The study of ion upflows starts with calculation of a quasi-stationary initial state, similar to SR12.

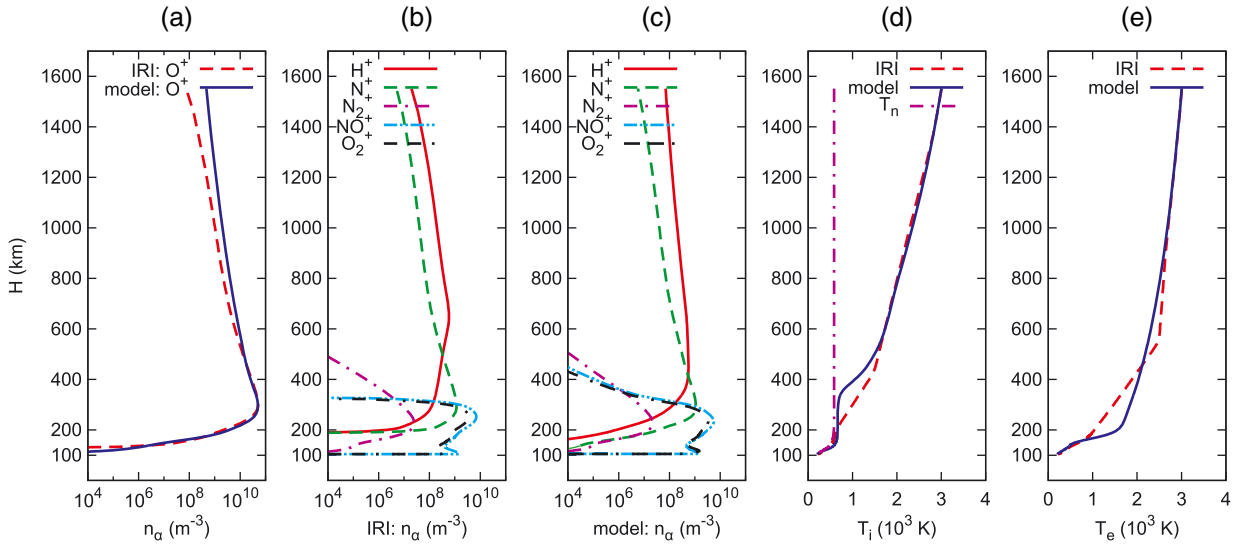

Figure D1. Vertical profiles of the following values. (a) O^+ ion density provided by IRI (dashed red) and the quasi-stationary O^+ density (solid blue). (b) Densities of all ion species except O^+ provided by IRI. (c) Quasi-stationary densities of all ion species except O^+. (d) Temperature of neutrals (dash-dotted magenta), ion temperature provided by IRI (dashed red), and the quasi-stationary ion temperature (solid blue). (e) Electron temperature provided by IRI (dashed red) and the quasi-stationary electron temperature (solid blue). All profiles are obtained along the middle geomagnetic field line of the main simulation area.

The electron temperature and the ion densities and temperature are initialized with data provided by IRI-2007 (IRI, International Reference Ionosphere, 2007, http://nssdcftp.gsfc.nasa.gov/models/ionospheric/iri/iri2007/) for 6 A.M., 01 January 2007, at geomagnetic latitude and longitude of 72° and 335°, respectively. Parameters of the neutral atmosphere are provided by MSIS-86 (A. E. Hedin, Mass-Spectrometer-Incoherent-Scatter (MSIS) neutral atmosphere model, 1987, http://nssdcftp.gsfc.nasa.gov/models/atmospheric/msis/msis86/). It is found that with the original O^+ density (dashed red curve in Figure D1a), the upward velocity of O^+ ions reaches 1000 m/s near the top boundary. The acceleration is caused by the strong pressure gradient. In order to avoid a strong O^+ ion upflow in the quasi-stationary state, the initial O^+ ion density is increased above 380 km so that the right-hand side of equation (5) is

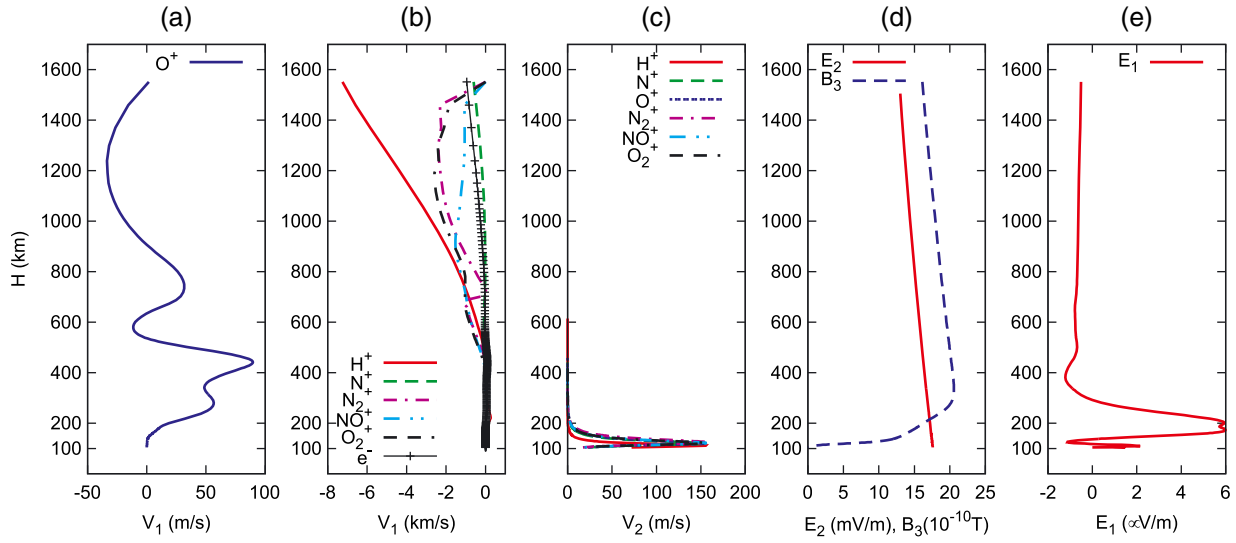

Figure D2. Vertical profiles of the following quasi-stationary values. (a) O^+ ion flow velocity along the geomagnetic field. (b) Flow velocities along the geomagnetic field for electrons and all ion species except O^+. (c) Ion flow velocities across the geomagnetic field in the meridional direction. (d) Transverse electric (solid red) and magnetic (dashed blue) fields. (e) Parallel electric field. In Figures D2a, D2b, and D2e, positive values are directed downward. All profiles are obtained along the middle geomagnetic field line of the main simulation area.

zero (see the solid blue curve in Figure D1a). The balance of forces for O^+ is calculated with zero ion flow velocities and the profiles of ion temperature and densities of other ion species given by the IRI model. After the initialization, the system is allowed to evolve for 120 s without any external perturbation. During this time, ion densities change due to field-aligned convection and chemical reactions (compare initial density profiles in Figure D1b with final profiles in Figure D1c). Significant changes take place at lower altitudes in ion (Figure D1d) and electron (Figure D1e) temperatures. The O^+ ion field-aligned flow velocity remains relatively small, below 100 m/s (see Figure D2a). The velocities of other ions are quite large above 400 km (see Figure D2b). However, at such altitudes, these ions are minor and their contribution to field-aligned current is small. Ion convection in the meridional direction is significant only below 200 km (see Figure D2c). The electromagnetic field components are shown in Figures D2d and D2e.

[62] **Acknowledgments.** The present study was supported by the Canadian Space Agency (CSA) and the National Sciences and Engineering Research Council of Canada (NSERC). The authors are thankful to Jean Pierre St.-Maurice for helpful discussions.

[63] Robert Lysak thanks Andrew Yau and William Lotko for their assistance in evaluating this paper.

References

Blelly, P. L., A. Robineau, D. Lummerzheim, and J. Lilensten (1996), 8-Moment fluid models of the terrestrial high latitude ionosphere between 100 and 3000 km, in *Solar-Terrestrial Energy Program: Handbook of Ionospheric Models*, edited by R. W. Schunk, pp. 53–72, Utah State University, Logan, UT and SCOSTEP, Boulder, CO.

Cladis, J. B. (1986), Parallel acceleration and transport of ions from polar ionosphere to plasma sheet, *Geophys. Res. Lett.*, *13*, 893–896.

Itikawa, Y. (2006), Cross section for electron collisions with nitrogen molecules, *J. Phys. Chem. Ref. Data*, *35*, 31–53.

Itikawa, Y. (2009), Cross section for electron collisions with oxygen molecules, *J. Phys. Chem. Ref. Data*, *38*, 1–20.

Liu, C., J. L. Horwitz, and P. G. Richards (1995), Effects of frictional ion heating and soft-electron precipitation on high-latitude *F*-region upflows, *Geophys. Res. Lett.*, *22*, 2713–2716.

Lynch, K. A., et al. (2007), Auroral ion outflow: Low altitude energization, *Ann. Geophys.*, *25*, 1967–1977.

Maeda, K. (1965), Diffusion of low energy auroral electrons in the atmosphere, *J. Atmos. Terr. Phys.*, *27*, 259–275.

Maeda, K., and A. C. Aikin (1968), Variations of polar mesospheric oxygen and ozone during auroral events, *Planet. Space Sci.*, *16*, 371–384.

Majeed, T., and D. J. Strickland (1997), New survey of electron impact cross sections for photoelectron and auroral electron energy loss calculations, *J. Phys. Chem. Ref. Data*, *26*, 335–349.

Ogawa, Y., S. C. Buchert, A. Sakurai, S. Nozawa, and R. Fujii (2010), Solar activity dependence of ion upflow in the polar ionosphere observed with the European Incoherent scatter (EISCAT) Tromsø UHF radar, *J. Geophys. Res.*, *115*, A07310, doi:10.1029/2009JA014766.

Rees, M. H. (1969), Auroral electrons, *Space Sci. Rev.*, *10*, 413–441.

Rees, M. H., A. I. Stewart, and J. C. G. Walker (1969), Secondary electrons in aurora, *Planet. Space Sci.*, *17*, 1997–2008.

Rees, M. H., R. A. Jones, and J. C. G. Walker (1971), The influence of field-aligned currents on auroral electron temperatures, *Planet. Space Sci.*, *19*, 313–325.

Sadler, F. B., M. Lessard, E. Lund, A. Otto, and H. Luhr (2012), Auroral precipitation/ion upwelling as a driver of neutral density enhancement in the cusp, *J. Atmos. Solar-Terr. Phys.*, *87-88*, 82–90.

Schunk, R. W. (1988), A mathematical model of the middle and high latitude ionosphere, *Pure Appl. Geophys.*, *127*, 255–303.

Seo, Y., J. L. Horwitz, and R. Caton (1997), Statistical relationships between high-latitude ionospheric *F* region/topside upflows and their drivers: DE 2 observations, *J. Geophys. Res.*, *102*, 7493–7500.

Staniforth, A., and J. Côté (1991), Semi-Lagrangian integration schemes for atmospheric models - A review, *Mon. Weather Rev.*, *119*, 2206–2223.

Strangeway, R. J., R. E. Ergun, Y.-J. Su, C. W. Carlson, and R. C. Elphic (2005), Factors controlling ionospheric outflows as observed at intermediate altitudes, *J. Geophys. Res.*, *110*, A03221, doi:10.1029/2004JA010829.

Streltsov, A. V., and W. Lotko (2008), Coupling between density structures, electromagnetic waves and ionospheric feedback in the auroral zone, *J. Geophys. Res.*, *113*, A05212, doi:10.1029/2007JA012594.

Su, Y.-J., R. G. Caton, J. L. Horwitz, and P. C. Richards (1999), Systematic modeling of soft-electron precipitation effects on high-latitude *F* region and topside ionospheric upflows, *J. Geophys. Res.*, *104*, 153–163.

Sydorenko, D., and R. Rankin (2012), Simulation of ionospheric disturbances created by Alfvén waves, *J. Geophys. Res.*, *117*, A09229, doi:10.1029/2012JA017693.

Sydorenko, D., R. Rankin, and K. Kabin (2008), Nonlinear effects in the ionospheric Alfvén resonator, *J. Geophys. Res.*, *113*, A10206, doi:10.1029/2008JA013579.

Tian, F., J. F. Kasting, H.-L. Liu, and R. G. Roble (2008), Hydrodynamic planetary thermosphere model: 1. Response of the Earth's thermosphere to extreme solar EUV conditions and the significance of adiabatic cooling, *J. Geophys. Res.*, *113*, E05008, doi:10.1029/2007JE002946.

Vontrat-Reberac, A., D. Fontaine, P.-L. Blelly, and M. Galand (2001), Theoretical predictions of the effect of cusp and dayside precipitation on the polar ionosphere, *J. Geophys. Res.*, *106*, 28,857–28,856.

Wahlund, J.-E., H. J. Opgenoorth, I. Haggstrom, K. J. Winser, and G. O. L. Jones (1992), EISCAT observations of topside ionospheric ion outflows during auroral activity: Revisited, *J. Geophys. Res.*, *97*, 3019–3037.

Williams, P. J. S., and J. N. McDonald (1987), Electron temperature and electron density in the *F*-region of the ionosphere. II. The role of atomic oxygen and molecular nitrogen, *J. Atmos. Terr. Phys.*, *49*, 873–877.

Yau, A. W., T. Abe, and W. K. Peterson (2007), The polar wind: Recent observations, *J. Atmos. Solar-Terr. Phys.*, *69*, 1936–1983.

Zhdanov, V. M. (2002), *Transport Processes in Multicomponent Plasma*, Taylor & Francis, London.